



HAL
open science

Combination of ICCD fast imaging and image processing techniques to probe species-specific propagation due to guided ionization waves

Dimitrios K Athanasopoulos, Panagiotis Svarnas, C M Liapis, Polycarpos K Papadopoulos, Kristaq Gazeli, Konstantinos Giotis, Panayiotis Vafeas, Georgios Vafakos, Vasileios Giannakakis, Alexandros Gerakis

► To cite this version:

Dimitrios K Athanasopoulos, Panagiotis Svarnas, C M Liapis, Polycarpos K Papadopoulos, Kristaq Gazeli, et al.. Combination of ICCD fast imaging and image processing techniques to probe species-specific propagation due to guided ionization waves. *Physica Scripta*, 2023, 98 (5), pp.055609. 10.1088/1402-4896/acc906 . hal-04054349

HAL Id: hal-04054349

<https://hal.science/hal-04054349>

Submitted on 19 Apr 2024

HAL is a multi-disciplinary open access archive for the deposit and dissemination of scientific research documents, whether they are published or not. The documents may come from teaching and research institutions in France or abroad, or from public or private research centers.

L'archive ouverte pluridisciplinaire **HAL**, est destinée au dépôt et à la diffusion de documents scientifiques de niveau recherche, publiés ou non, émanant des établissements d'enseignement et de recherche français ou étrangers, des laboratoires publics ou privés.



Distributed under a Creative Commons Attribution 4.0 International License



PAPER • OPEN ACCESS

Combination of ICCD fast imaging and image processing techniques to probe species-specific propagation due to guided ionization waves

To cite this article: D K Athanasopoulos *et al* 2023 *Phys. Scr.* **98** 055609

View the [article online](#) for updates and enhancements.

You may also like

- [Chaotic behavior of new experimental data of the LTGP \(2004-2006\) confirm possible relation to seismic activity in Western Greece](#)
K Giannakopoulos and A Ifantis
- [Exploiting unsupervised and supervised classification for segmentation of the pathological lung in CT](#)
P Korfiatis, C Kalogeropoulou, D Daoussis et al.
- [Integrating multiscale polar active contours and region growing for microcalcifications segmentation in mammography](#)
N S Arikidis, A Karahaliou, S Skiadopoulos et al.



PAPER

OPEN ACCESS

RECEIVED

9 November 2022

REVISED

9 February 2023

ACCEPTED FOR PUBLICATION

30 March 2023

PUBLISHED

11 April 2023

Original content from this work may be used under the terms of the [Creative Commons Attribution 4.0 licence](#).

Any further distribution of this work must maintain attribution to the author(s) and the title of the work, journal citation and DOI.



Combination of ICCD fast imaging and image processing techniques to probe species-specific propagation due to guided ionization waves

D K Athanasopoulos¹, P Svarnas¹, C M Liapis², P K Papadopoulos³, K Gazeli⁴, K Giotis^{1,4}, P Vafeas⁵, G P Vafakos³, V Giannakakis¹ and A Gerakis^{6,7,*}

¹ University of Patras, Department of Electrical and Computer Engineering, High Voltage Laboratory, 26504, Rion—Patras, Greece

² University of Patras, Department of Mathematics, 26504, Rion—Patras, Greece

³ University of Patras, Department of Mechanical Engineering and Aeronautics, 26504, Rion—Patras, Greece

⁴ Université Sorbonne Paris Nord, Laboratoire des Sciences des Procédés et des Matériaux, LSPM, CNRS, UPR 3407, F-93430, Villetaneuse, France

⁵ University of Patras, Department of Chemical Engineering, 26504, Rion—Patras, Greece

⁶ Texas A&M University, Department of Aerospace Engineering, College Station, Texas, 77843-3141, United States of America

⁷ Luxembourg Institute of Science & Technology, LIST, Belvaux L-4362, Luxembourg

* Author to whom any correspondence should be addressed.

E-mail: alexandros.gerakis@list.lu

Keywords: ICCD, plasma jets, plasma bullets, digital image processing, ICCD, UV-NIR filters

Abstract

The present report is devoted to the study of distinct ionization waves in terms of temporally-, spatially-, and wavelength-resolved analyses. The study is based on the technique of two-dimension fast imaging. However, appropriately selected ultraviolet to near infrared optical filters are employed to capture the propagation of specific species and digital image processing techniques are applied to explore the recorded snapshots. N_2 (SPS), N_2^+ (FNS), He I, OH(A–X), and O I, i.e., emissive neutral and ionic species, are investigated. On the other hand, the propagation of the NO_γ species is studied by means of laser-induced fluorescence spectroscopy, since the light intensity due to spontaneous emission of this species was not readily detectable. Digital image processing techniques are also applied for the NO_γ case. The crucial role of the above species in fields like plasma biomedicine and material processing is extensively recognized, and the present work: (i) provides gathered information on the propagation of these species within the atmospheric air; and (ii) introduces image processing algorithms to extract information which otherwise would remain hidden or uncorrelated with other plasma parameters. The present results unveil specific emission patterns due to the propagation of the N_2 (SPS), N_2^+ (FNS), He I, OH(A–X), and O I species. The intensity patterns consist of a first peak located in the vicinity of the reactor orifice, a second peak moving away from the reactor orifice, and a continuum which couples the two peaks. However, the detailed features of each pattern depend on the type of species considered. The fluorescence of the NO_γ species also suggests the division of the area downstream of the reactor orifice into two regions where distinct ionization–excitation effects take place. Propagation speeds of the species up to about $2 \times 10^5 \text{ m s}^{-1}$ were measured. Finally, qualitative correlation between the species propagation (as it is pronounced by the emission patterns) and the local electric field (as it was numerically calculated in a similar setup) is demonstrated.

1. Introduction

Atmospheric pressure plasmas in the form of plasma jets operate usually with noble gases in ambient conditions, driven by either sinusoidal or pulsed high voltages. Being out of thermodynamic equilibrium, these plasmas meet the criteria for various targeted applications, mostly due to the high yield of reactive oxygen and nitrogen species (abbreviated to ‘RONS’) [1]. RONS are produced during the propagation of ultrafast ionization waves.

The latter are pictorially described as ‘plasma bullets’, have a carrot-like shape, properties resembling in many ways to streamers, and typical propagation speeds ranging from 10^4 to 10^6 m s⁻¹ [2]. Particularly, pulsed-driven helium (He) plasma jets have gained extensive attention for a variety of applications, with a special focus on the plasma biomedicine field [3]. The special interest in the helium gas arises from its high ionization coefficient at relatively low reduced electric fields [4], while the interest in pulsed driven plasma jets is justified by their efficiency in terms of chemical reactivity and power consumption [5].

In such cases, the study of the ionization waves and the produced RONS, in terms of identification, kinetic reactions, and dynamics, are of critical importance. Therefore, optical emission spectroscopy (OES) and fast intensified charge-coupled device (ICCD) imaging are usually employed to probe these waves. On the other hand, laser-induced fluorescence (LIF) represents a non-intrusive, species-specific, temporally- and spatially-resolved approach to probe plasmas. LIF operates on the principle that when a particle in a lower energy state absorbs a photon and rises to a higher energy state, it will de-excite and emit another photon. Laser-excited particles will decay by collision, spontaneous emission, or stimulated emission. This spontaneous emission, or fluorescence, radiates isotropically away from the particle and it can be detected as a footprint of the probed particle [6].

Consequently, many works have focused on the dynamics of helium pulsed plasma jets. Ultimate aims of these works are the enhancement of the reactive species production and the understanding of their propagation mechanisms. Cases of plasma jets that expand freely in air or impinge on substrates [7–12], have both been considered. Key results based on (i) ICCD and bandpass optical filters [8, 12–14], (ii) LIF [7, 8, 15–17], (iv) ICCD and LIF combination [9–11, 18–21], ICCD and two-photon absorption LIF (TALIF) combination [11, 21], and (v) OES [9, 12, 22–24] have been reported. These works highlight the interest and progress in the field.

Accordingly, our group has studied ionization waves triggered by atmospheric pressure helium plasma jets [2]. In that preliminary work, the plasma jet was driven by sinusoidal high voltage, and the main topic was the demonstration of the uncertainties introduced during the use of ICCD fast imaging by the inherently erratic propagation of the waves. The wavelength integrated emission had then been considered only. On the contrary, the present work refers to pulsed helium plasma jet, and presents a systematic combination of wavelength filtered fast imaging and LIF fast imaging with digital image processing techniques. It is admitted that both techniques have been applied to plasma jets since at least one decade (see for instance [8, 12–14] and [9–11, 18–21], respectively), but their combination with image processing algorithms becomes the main claim of the present work. It is argued that the naked eye observations of the ICCD snapshots—raw images of ‘plasma bullets’, regularly presented in the literature—may lead to loss of information or even mistaken conclusions. It is here demonstrated that image processing tools may mitigate such issues, allow the accurate evaluation of different physical parameters (e.g., ionization wave speed, reactive species relative density, etc), and facilitate the correlation of experimental and numerical data. ICCD fast imaging, optical filters, LIF, and digital image processing algorithms are coupled, and a conclusive picture on the spatiotemporal evolution of many RONS is obtained. The results are presented in detail and eventually discussed.

2. Experimental setup

2.1. Plasma jet system

Figure 1 depicts the concept of the experimental setup used for the plasma production and characterization. The design of the plasma jet reactor is based on a coaxial dielectric-barrier discharge (DBD) configuration.

This reactor has been successfully employed for bacterium inactivation [25], human skin treatment [26], liposome disruption [27, 28], and other studies in the field of plasma biomedicine. It comprises of: (i) a capillary alumina tube ($\varnothing_{\text{out}} = 2.5$ mm; $\varnothing_{\text{in}} = 1.14$ mm; length of 80 mm) acting as the dielectric barrier; (ii) a thin wire internal electrode (made of tungsten; $\varnothing = 0.125$ mm) inserted into the tube and terminated 20 mm behind the tube orifice; and (iii) a cylindrical hollow external electrode (made of brass; $\varnothing_{\text{out}} = 10$ mm; length of 10 mm) tightly fixed around the tube. Its outer edge is placed 20 mm behind the tube orifice, thus forming a 10 mm in length coaxial DBD with the internal electrode. The internal electrode is the driven one while the external is grounded directly. Thus, two self-sustained discharges are formed, as figure 1 depicts. The first one is a radial DBD inside the dielectric barrier and the second one refers to a plasma jet, i.e., ionization waves propagating between the wire pin and any virtual ground in the reactor vicinity. The ionization waves are guided by the dielectric tube and the fluid channel formed by the helium gas [29–31].

The working gas is high purity helium (He; 99.999%) and it is introduced into the dielectric tube through a mass flow meter (set at 2 standard liters per minute). The distance between the reactor orifice and the surface of the grounded optical table hosting the experimental set up is set at 190 mm.

The driving voltage is generated by a custom-made pulsed power supply based on metal-oxide-semiconductor field-effect transistor (MOSFET) technology [32, 33]. The pulsed high voltage is constantly

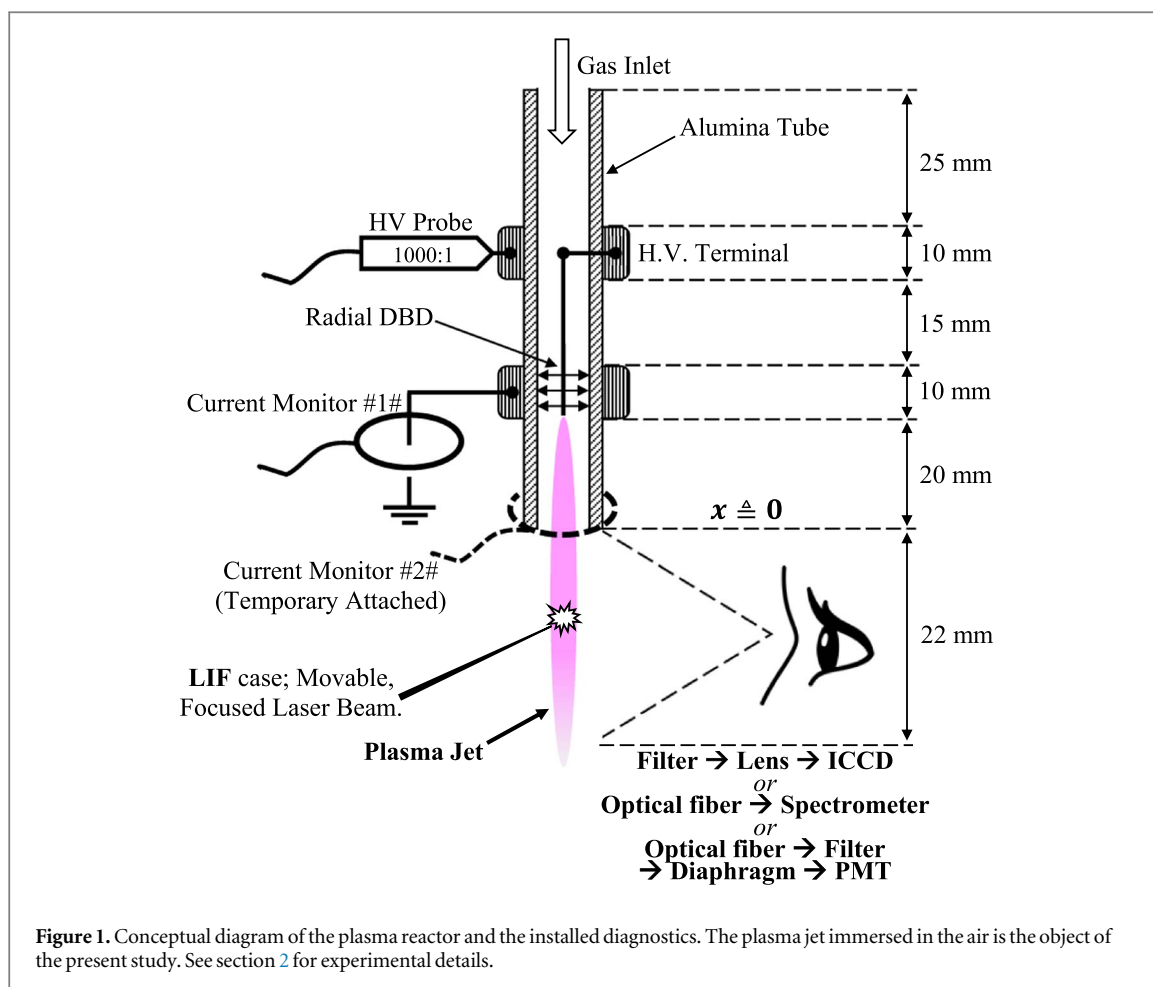


Table 1. Indicative specifications of the optical components used for the PMT experiments.

Species	Filter Model	Transition	Wavelength	Transmittance (approx.)			
				Filter	Fiber	PMT	Total
N ₂	Thorlabs FB340	C ³ Π _u → B ³ Π _g	337.1 nm	25%	58%	25%	3.6%
N ₂ ⁺	Thorlabs FB390	B ² Σ _u ⁺ → X ₂ Σ _g ⁺	391.4 nm	30%	59%	24%	4.2%
He	Thorlabs FB710	3 ³ S ₁ → 2 ³ P _{0,1,2}	706.5 nm	50%	54%	5%	1.3%
O	Thorlabs FB780	3p ⁵ P → 3s ⁵ S	777.3 nm	50%	54%	3.5%	0.9%
OH	Edmund 34–976	A ² Σ ⁺ → X ² Π	309 nm	60%	57%	25%	8.5%

measured with a voltage divider (1000:1; DC-75 MHz) and it refers to an amplitude of +5 kV, a repetition frequency of 2 kHz, and a pulse plateau of 420 ns. Two current transformers (400 Hz to 250 MHz) are employed to record both the radial and axial currents, as it is shown in figure 1 (monitors #1# and #2#, respectively). Monitor #1# records the sum of two current components, i.e., the displacement current due to the reactor capacitance and the drift current due to the DBD itself. The first component is subtracted from the total current, yielding the DBD current, as it is explained in the [appendix](#). Monitor #2# is removed during any optical measurement since otherwise it intervenes in the field of view.

Furthermore, a photoelectron multiplier tube (PMT; Hamamatsu R928; 185–900 nm) is used for routine optical observations as a function of time. The optical emission from a cone of base diameter of 22 mm (figure 1) is captured by a high-grade fused silica fiber optic bundle (MKS-Newport; 77576) and guided to the PMT. Case-by-case, pinhole diaphragms are added to prevent photocathode saturation and obtain linear response. Optical filters allow for the selective detection of emissive species, according to the transitions and the specifications of table 1. It is noted that, the data of table 1 are indicatively given by the providers, and they do not correspond to any further calibration. All waveforms are monitored on a digital oscilloscope (400 MHz; 5 GSamples s⁻¹).

Special attention is paid to the voltage, current, and PMT signal shifting. Shifting corrections are carried out by measuring the propagation delay imposed by the coaxial cables of these units to a reference TTL pulse. In

Table 2. Indicative specifications of the optical components used for the ICCD experiments.

Species	Filter Model	Transition	Wavelength	Transmittance (approx.)			
				Filter	Lens	ICCD	Total
N ₂	Thorlabs FB340	C ³ Π _u → B ³ Π _g	337.1 nm	25%	95%	11%	2.6%
N ₂ ⁺	Thorlabs FB390	B ² Σ _u ⁺ → X ₂ Σ _g ⁺	391.4 nm	30%	90%	13%	3.5%
He	Thorlabs FB710	3 ³ S ₁ → 2 ³ P _{0,1,2}	706.5 nm	50%	30%	4%	0.6%
O	Thorlabs FB780	3p ³ P → 3s ³ S	777.3 nm	50%	30%	3%	0.45%
OH	Edmund 34–976	A ² Σ ⁺ → X ² Π	309 nm	60%	90%	12%	6.5%
No _γ (LIF)	Semrock FF01–260	X ² Π → A ² Σ ⁺ (excitation) A ² Σ ⁺ → X ² Π (fluorescence)	252–268 nm	60%	90%	5%	2.7%

addition, the delay of the voltage-probe head itself, and the PMT transit time plus its anode rise time, are considered. Any delay due to the current transformer head itself is ignored (useable rise time 1.5 ns).

Furthermore, due to the ns-rising part of the high voltage pulse, background noise is induced and disturbs the PMT signals. This background is recorded by masking the PMT and it is then subtracted from the raw signal. A typical latency of 5 ns is also assumed for the fiber optic bundle.

A portable spectrometer of low resolution (AvaSpec; ULS4096CL-EVO-UA-10) serves to explore the optical emission wide spectrum of the plasma jet (22 mm field of view; figure 1). It is equipped with a 300 grooves mm⁻¹ grating (200–1100 nm; blaze 300 nm) and a CMOS photodetector (4096 pixel). The light is led to the unit by means of a fused silica optical fiber (200–2500 nm; NA 0.22). Wavelength calibration is carried out with an Hg(Ar) pencil-style lamp. Attention is given to calibrate the relative spectral efficiency of the entire optical system. This is accomplished with a quartz-tungsten-halogen lamp (250 W) operated at the color temperature of 3400 K.

2.2. Fast imaging—optical filters

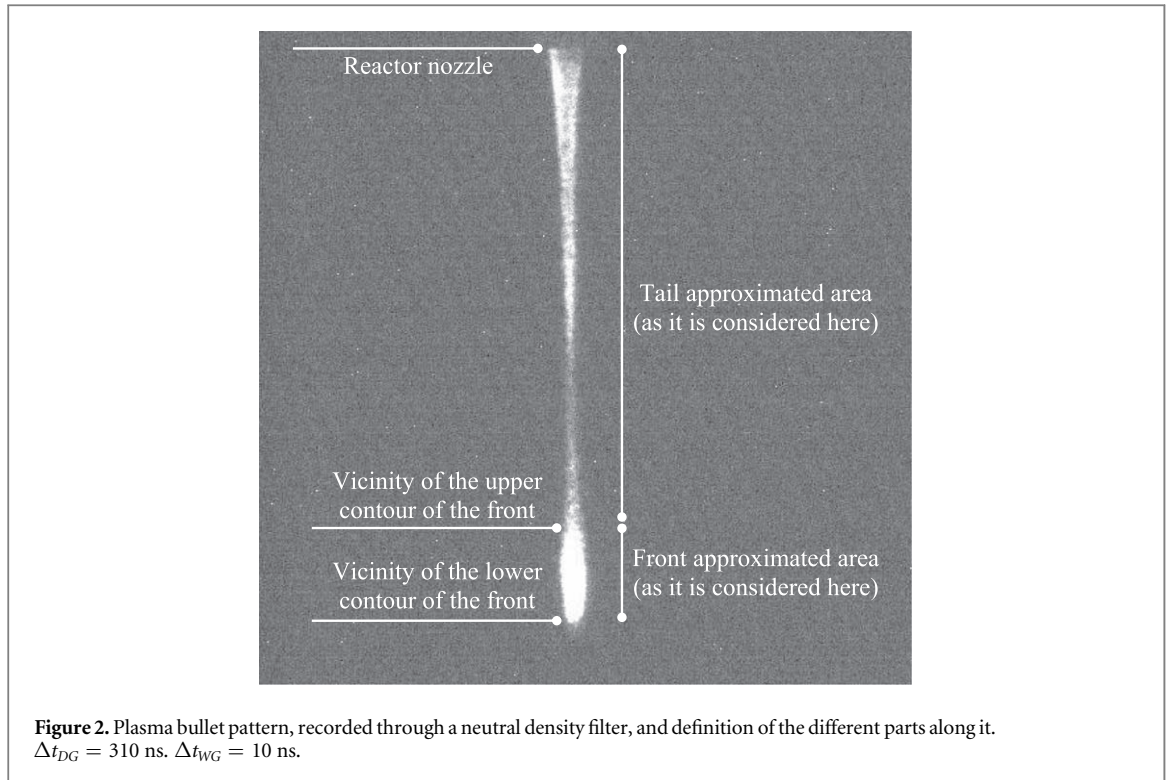
The spatiotemporally resolved detection of the emissive species is carried out with wavelength filtered fast imaging. The transitions under consideration and the spectral features of the associated filters are given in table 2 (see reference [34] for further details). These species are selected as the principal ones, based on previous [35–37] and current (see section 4.1) OES experiments of our group. The detector is an ICCD (Princeton Instruments; PI-MAX4 1024i; Gen II Intensifier; RB Fast Gate), equipped with a suitable lens (SODERN; UV Cerco[®] 2178). Table 2 provides approximated values of the relative optical transmittance due to the ICCD and the lens, based on the manufacturers' datasheets without any further calibration. The last column of the table gives roughly the aggregated attenuation involved in the detection of each species.

The probed zone is 22 mm vertically, starting from the reactor orifice which is arbitrarily defined as the position of $x_o = 0$ mm (figure 1). A 4-channel digital delay/pulse generator (Stanford Research Systems Inc.; DG645) triggers the power supply and the ICCD camera. The ICCD gate is thus triggered at different instants (Δt_{DG}) with respect to the rising part of the high voltage pulse. Δt_{DG} is accurately measured by observing the ICCD gate-monitor output on the oscilloscope. The shifts imposed by the high voltage probe, the ICCD transit time, and the coaxial cable connecting the ICCD gate-monitor output to the oscilloscope are offset. Following various tests, the ICCD gain is maintained at the level of 100, and the gate width (Δt_{WG}) is maintained at 10 ns as a compromise between increased spatiotemporal resolution and increased signal-to-noise ratio in the snapshots. Previously published practical and theoretical considerations on the use of ICCD imaging [38] have been taken into account.

2.3. Fast imaging—laser-induced fluorescence

Contrary to the abovementioned species, the NO_γ species is not readily detectable in plasma jets while it is strongly dependent on the gas additives [36]. However, its role in biochemical applications is decisive [39]. Thus, LIF is employed for its spatiotemporal detection.

For the excitation of the NO_γ species, a dye laser (Sirah; Cobra) using Coumarin 450 is used. It is pumped at 355 nm by a Nd:YAG laser (Spectra-Physics; Quanta-Ray Lab-series). The resultant laser pulse has a frequency of 10 Hz, width of 10 ns, wavelength at 226.803 nm, and energy of about 800 μJ. The latter is continuously monitored to be maintained as constant as possible, thus making the acquired LIF signals comparable in terms of relative units. The laser beam is guided by mirrors and focused onto the plasma jet vertical axis by a biconvex lens (laser spot less than 1 mm in diameter). The laser pulse signal is recorded by a fast photodiode placed behind the plasma jet. The induced NO_γ transition is the X²Π($v' = 0$) → A²Σ⁺($v'' = 0$) [40, 41] and the subsequent fluorescence light (250–260 nm) is detected perpendicular to the laser beam. The detector is the previously mentioned ICCD, masked by a band pass optical filter (252–268 nm; see table 2).



The 4-channel digital delay/pulse generator mentioned above is again employed. Hence, the power supply, the laser lamp, the laser Q-switch, and the ICCD gate are cross-triggered at a frequency of 10 Hz. Since the driving voltage is set at 2 kHz, LIF records are acquired every two hundred (200) periods of the driving voltage.

2.3.1. LIF on the plasma bullet front

The desired spatial resolution along the vertical position x is chosen (2 mm here). Δt_{DG} is adjusted, with respect to the rising part of the high voltage pulse, to capture the vicinity of the lower contour of the bullet front (figure 2) at any considered vertical position x_i . The laser lamp and Q-switch are triggered so that the 10-ns laser pulse overlaps the ICCD gate pulse; in other words, the 10-ns photodiode signal is seen within the Δt_{WG} gate width. The laser beam is then moved (micro-stepping by means of a translation stage) until it is focused on the considered vertical position x_i . Eventually, the laser lamp/Q-switch triggering is fine-tuned until the LIF intensity is maximal locally. The above procedure is repeated as many times as the number of the vertical positions of interest ($i = 0, 1, 2, \dots$). The ICCD gain is maintained constant at the level of 100 and the gate width (Δt_{WG}) at 30 ns.

2.3.2. LIF on the plasma bullet tail

The desired spatial resolution along the vertical position x is chosen (1 mm here). Δt_{DG} is adjusted to capture the vicinity of the upper contour of the bullet front (figure 2)—i.e., the vicinity of the lower contour of the bullet tail—slightly before it leaves the field of view of the camera. Thereafter, Δt_{DG} is fixed at this value. The laser lamp and Q-switch are triggered so that the 10-ns laser pulse overlaps the ICCD gate pulse. Thereafter, the laser lamp/Q-switch triggering remains unchanged. The laser beam is then moved to be focused on each of the considered vertical position x_j progressively ($j = 0, 1, 2, \dots$). The ICCD gain is set at the level of 100 and the gate width Δt_{WG} at 30 ns.

3. Image and signal processing

3.1. Fast imaging—optical filters

For the efficient exploitation of the captured snapshots, digital image processing techniques are applied. All images are converted to matrices of size 1024×1024 pixels, with a lab-made Python code. Each pixel carries out a value between 0 (black) and 65535 (white), indicating grayscale images. For consistency reasons and noise reduction, 3 series of experiments are carried out. This provides 3 snapshots at each time point which are then averaged to generate a single matrix. This is accomplished by adding the matrices of the individual images and

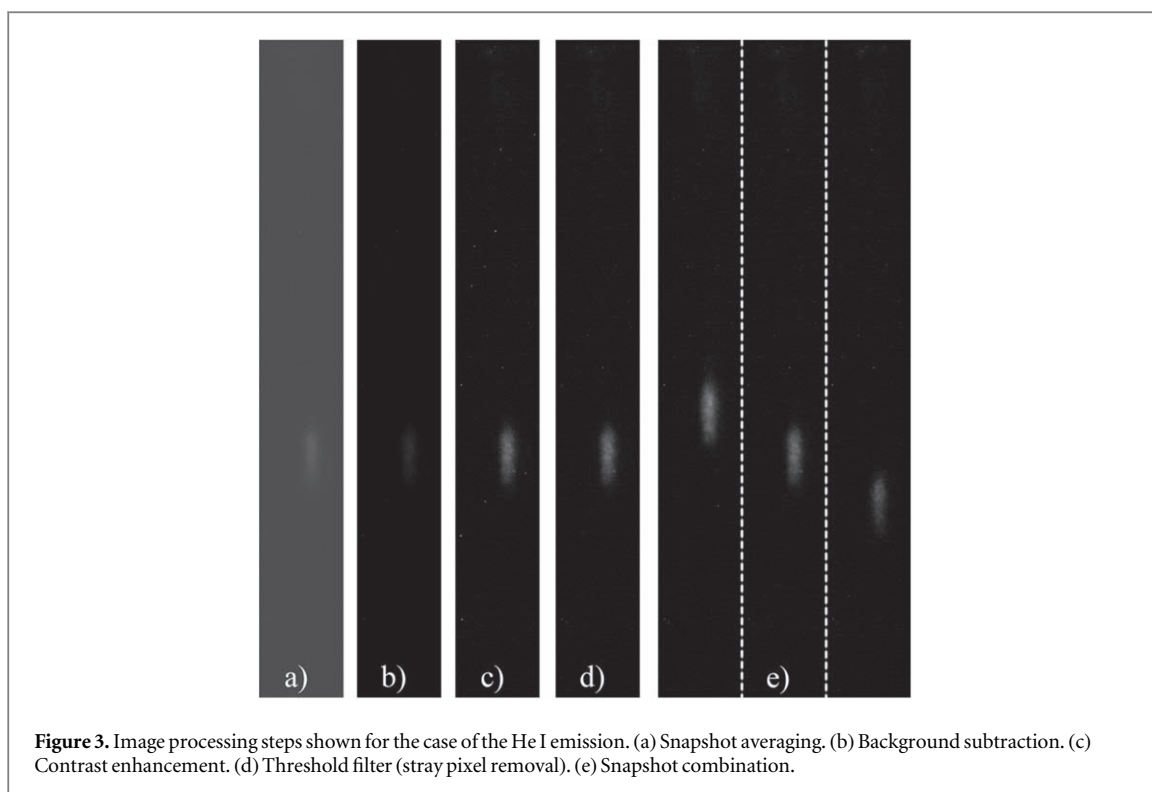


Figure 3. Image processing steps shown for the case of the He I emission. (a) Snapshot averaging. (b) Background subtraction. (c) Contrast enhancement. (d) Threshold filter (stray pixel removal). (e) Snapshot combination.

subsequently dividing them by 3 (figure 3(a)). The background noise is removed by subtracting 3 averaged snapshots captured with the plasma being ‘off’. A representative resulting image is shown in figure 3(b).

To visualize the emission, once the background has been subtracted, the contrast is enhanced by a certain factor (figure 3(c)). This factor is different for each emissive species, but it is maintained constant among all the snapshots of the same species. Threshold filters (one sharpened threshold per emissive species) are then applied to further reduce the noise (e.g., stray gray pixels) in the inert area (figure 3(d)). The threshold level is determined as a compromise between high noise reduction and low data distortion. Finally, snapshots from different Δt_{DG} are combined (figure 3(e)).

On the other hand, for the emission presentation by means of plots, images are averaged, the background is subtracted, and threshold filters are applied (figure 4(a)). Subsequently, the entries of each image matrix are averaged along each row and the light intensity as a function of the vertical distance x is obtained (figure 4(b)). The resulting data may demonstrate some fine-scale value variations (see stray peaks in figure 4(b)). Thus, they are smoothed out using a moving average filter (averaging window of 10) (figure 4(c)). This smoothing process is necessary, especially in the cases of low signal-to-noise ratio such as the images from the atomic oxygen detection.

3.2. Fast imaging—laser-induced fluorescence

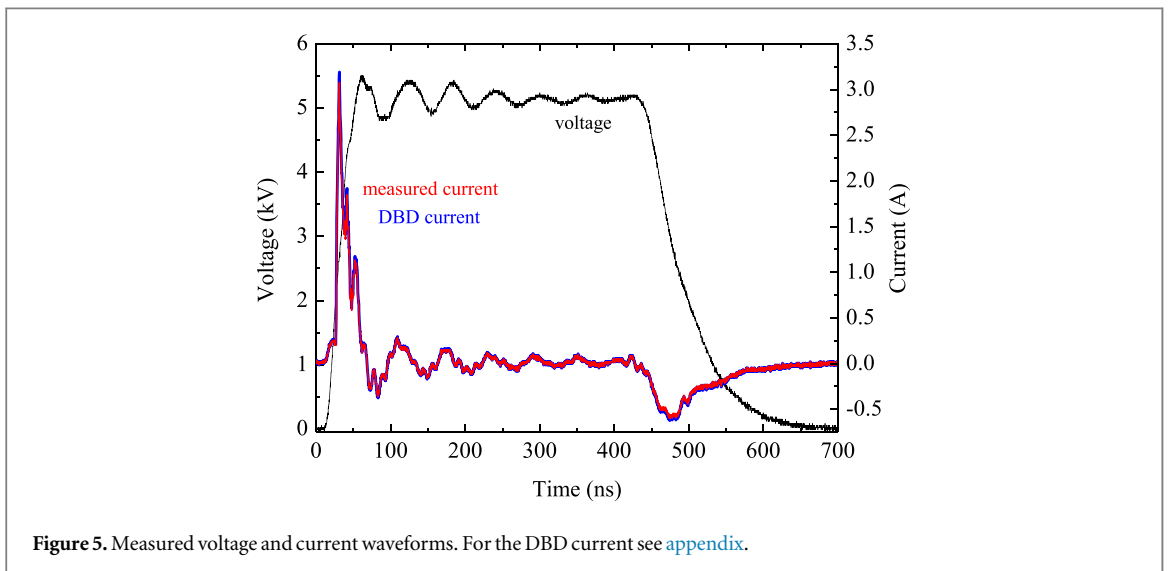
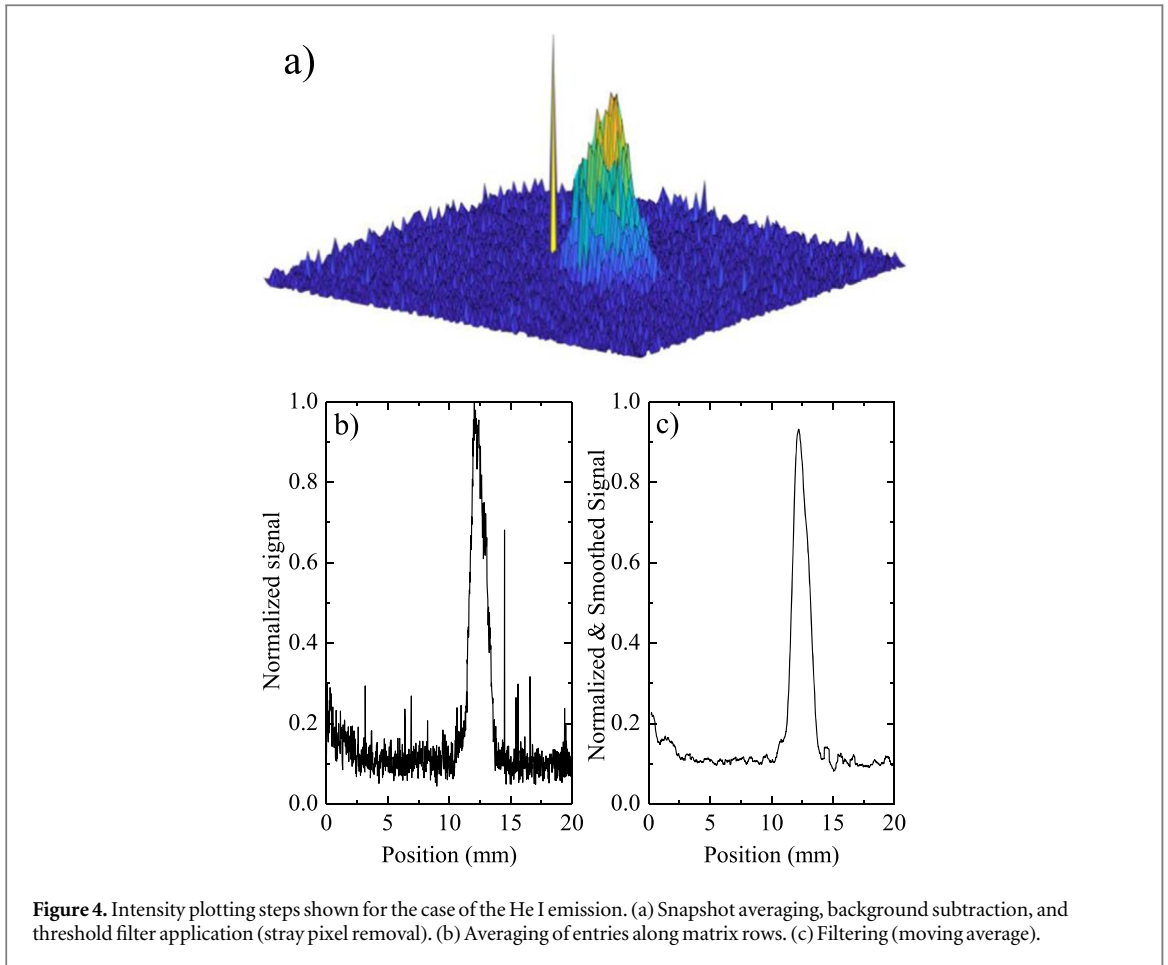
A similar approach is followed to obtain images and plots corresponding to the fluorescence of the NO_γ species. In this case, 10 snapshots are captured at each position x , which are subsequently averaged. The background noise is removed using 10 averaged snapshots captured with the plasma being ‘off’. The rest processing steps are the same to the ones mentioned above (section 3.1).

4. Results

4.1. Electrical and optical features

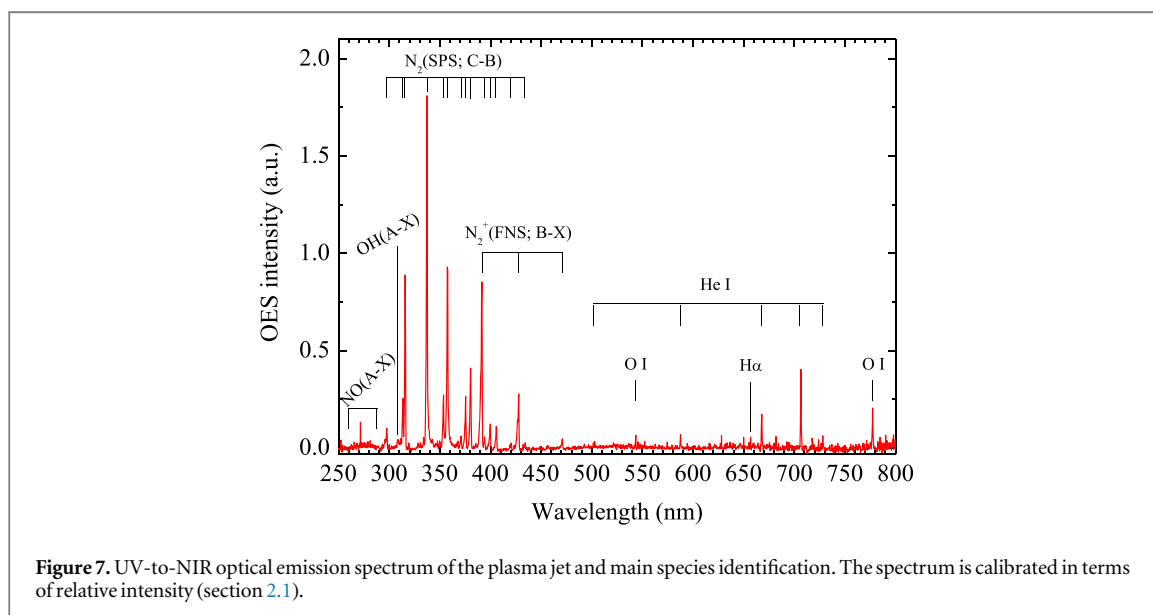
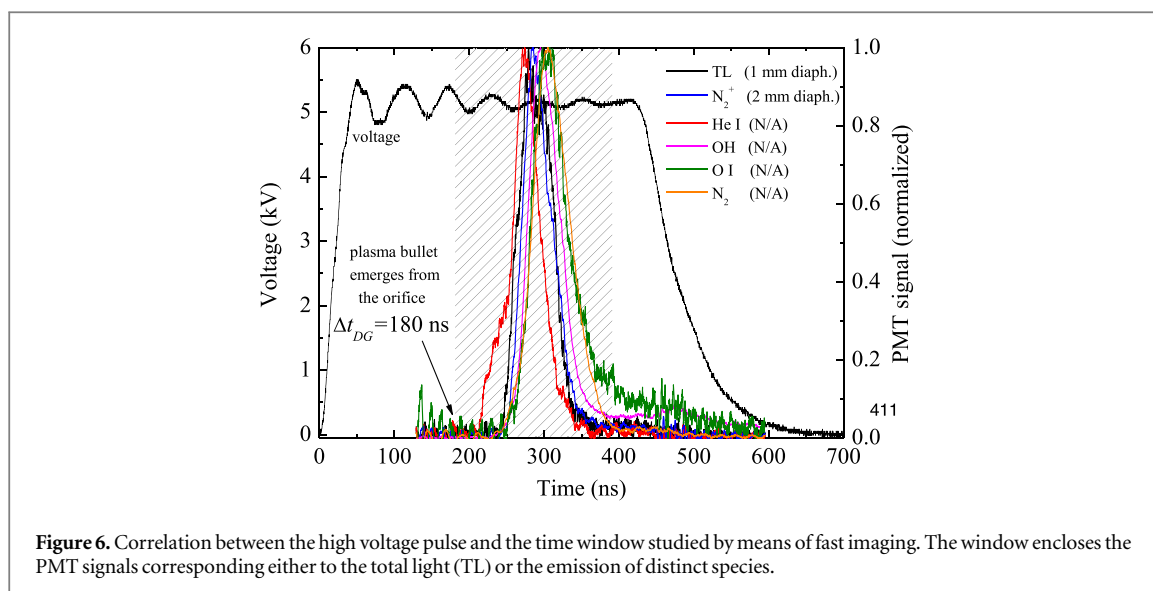
Figure 5 presents representative waveforms of the driving voltage pulse and the induced DBD current. The DBD current is evaluated from the signal of the monitor #1# in figure 1 and according to the notions discussed in the appendix. The plasma jet current may be found by the signal of the monitor #2# [42]. However, in our case it was comparable to the noise produced by the high voltage burst. Thus, its waveform is not shown here. However, routine filtering of the noisy signals implied a current peak less than 3 mA.

Figure 6 shows the temporal correlation between the high voltage pulse and the emission of the different species, based on the wavelength filtered PMT signals. The latter are reduced to their maximal value. In addition, the wavelength-integrated light (total light; TL) is recorded. All signals lag the high voltage pulse by about 200 ns.



This delay corresponds to the time needed for the plasma bullet to propagate along the 20-mm path between the inner electrode tip and the dielectric tube orifice (figure 1). This leads roughly to a mean speed of about 10^5 m s^{-1} . Besides, the alumina tube is not transparent. Hence, any optical emission study, either inside or outside the alumina, earlier than about 200 ns is beyond consideration. Moreover, the falling part of the high voltage pulse is associated with relatively negligible optical emission (figure 6). Thus, these constraints guide the present study over the plateau of the voltage pulse only. This time window is implied in figure 6 by the patterned area.

According to the ICCD fine triggering, the above delay is 180 ns. Namely, the emission in the vicinity of the reactor orifice becomes detectable for $\Delta t_{DG} \geq 180 \text{ ns}$, independently of the filter used. This value was also confirmed when we focused on the beginning of the TL signal of the PMT. The signals of figure 6 are plotted as



normalized since they are not calibrated in terms of emission intensity, but they have different signal-to-noise ratios. This may mislead to the above discrepancy (i.e., 200 ns instead of 180 ns). In any case, apart from the filters, the components involved in the PMT and ICCD experiments have different specifications (tables 1 and 2, respectively), making the direct comparison of the corresponding results tricky. Hereafter, the plasma bullets is assumed to emerge from $x_0 = 0$ mm when $\Delta t_{DG} = 180$ ns.

Figure 7 provides a wide scan of the optical emission spectrum of the plasma jet under the present experimental conditions. In the same figure the detected species are identified. The choice of the species considered in the present work is thus justified.

4.2. Emissive species

Figure 8 illustrates the plasma bullet propagation as it is mirrored on the corresponding emission. The time points refer to Δt_{DG} . As mentioned previously, $\Delta t_{WG} = 10$ ns. Figure 8(a) corresponds to the propagation pattern produced when the wavelength-integrated emission (TL) is considered. On the contrary, in figures 8(b) to (f) the emission of specific species is considered, i.e., OH, N₂, N₂⁺, He I, and O I, respectively. In all cases, an ionization wave confined in a quasi-cylindrical channel is initially formed, whereas it is progressively transformed to a ‘front - tail’ structure as it propagates. The front is gradually separated from the tail and the latter fades out for increasing propagation times. However, figure 8(f) (where the emission is weak, and pixels of

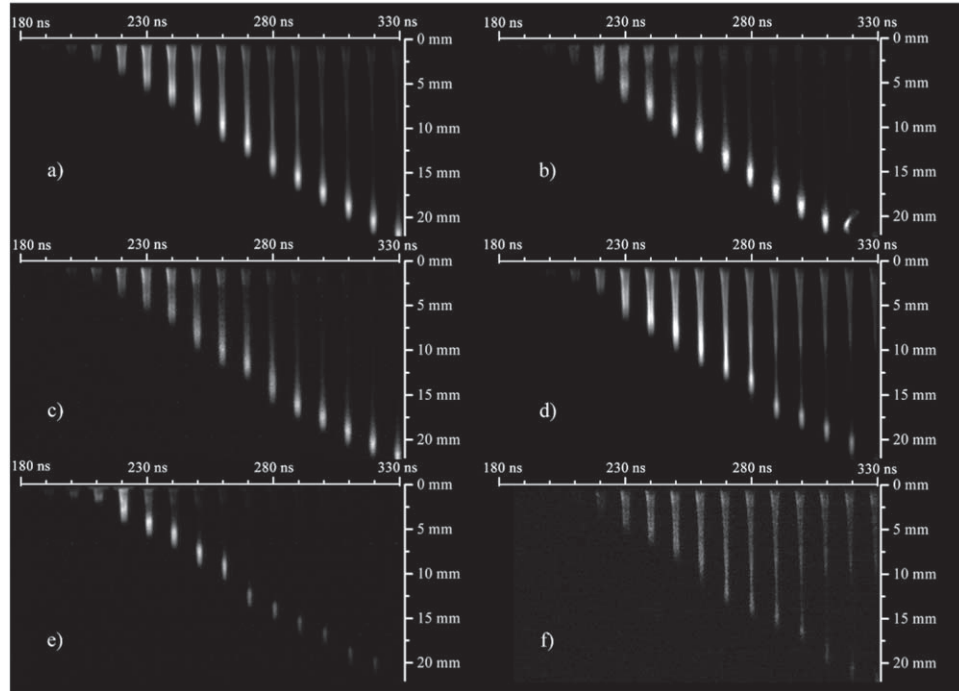


Figure 8. Spatiotemporally resolved patterns of the emission induced during electron avalanche propagation. (a) Wavelength-integrated emission (TL). (b) OH emission. (c) N_2 emission. (d) N_2^+ emission. (e) He I emission. (f) O I emission. The mentioned times correspond to Δt_{DG} ; $\Delta t_{WG} = 10$ ns.

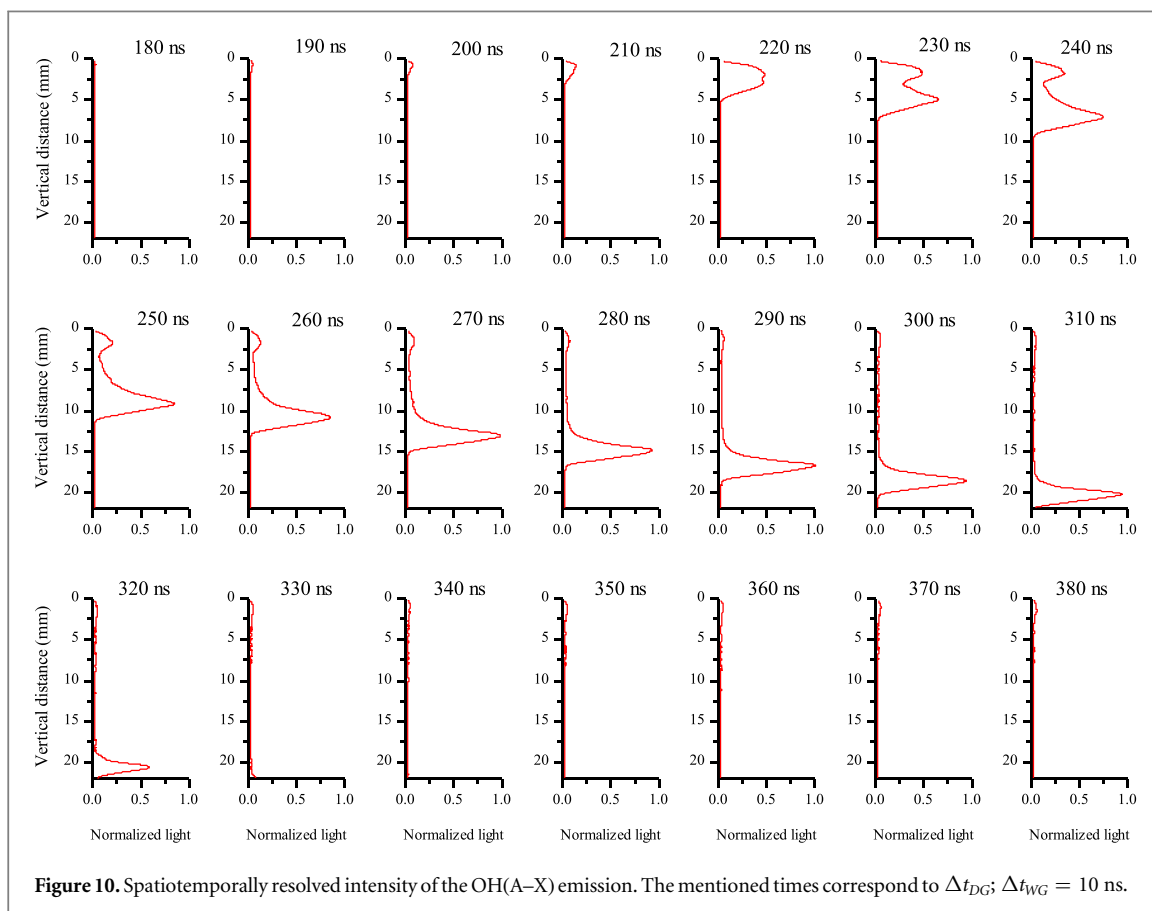
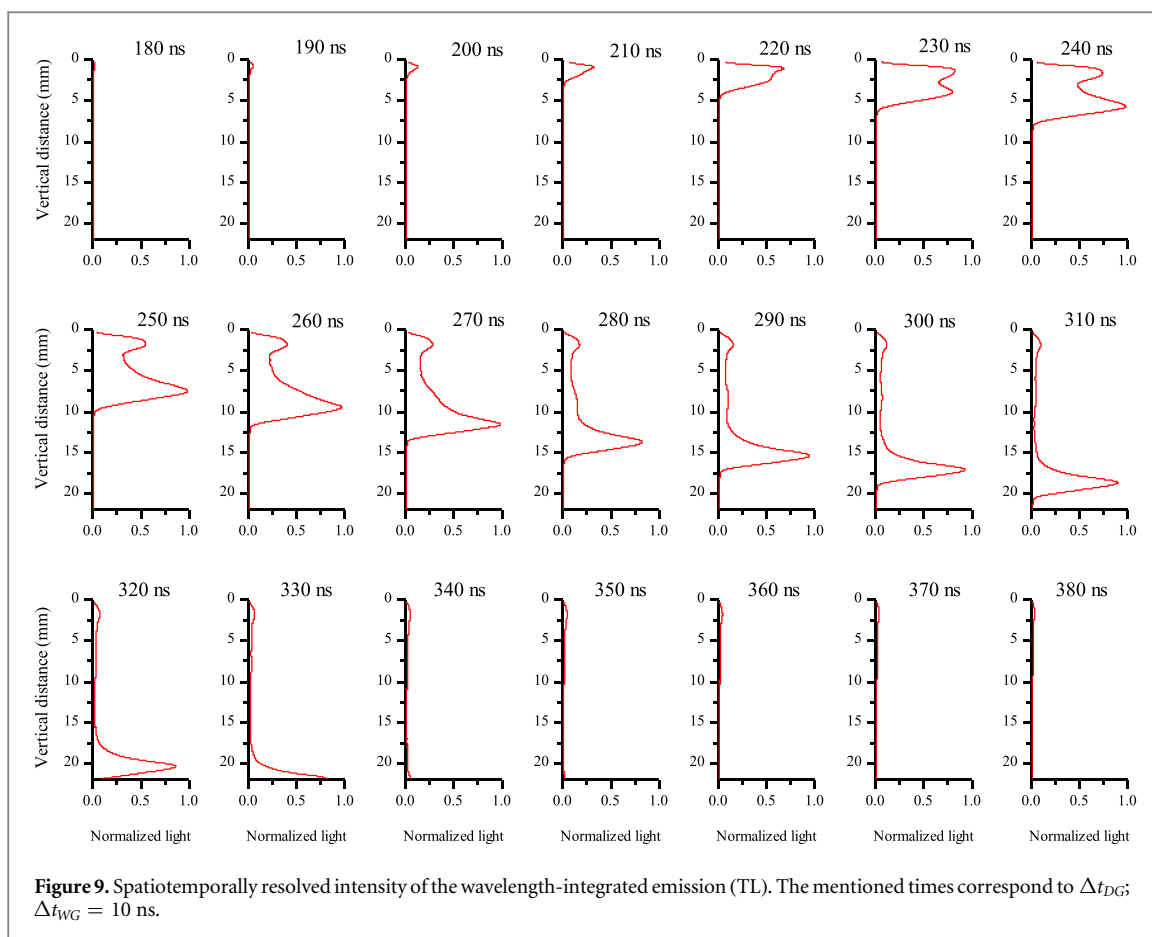
low values are not veiled) reveals that the tail forms a residual channel between the reactor orifice and the bullet front. This is better demonstrated by further image processing which leads to figures 9–14.

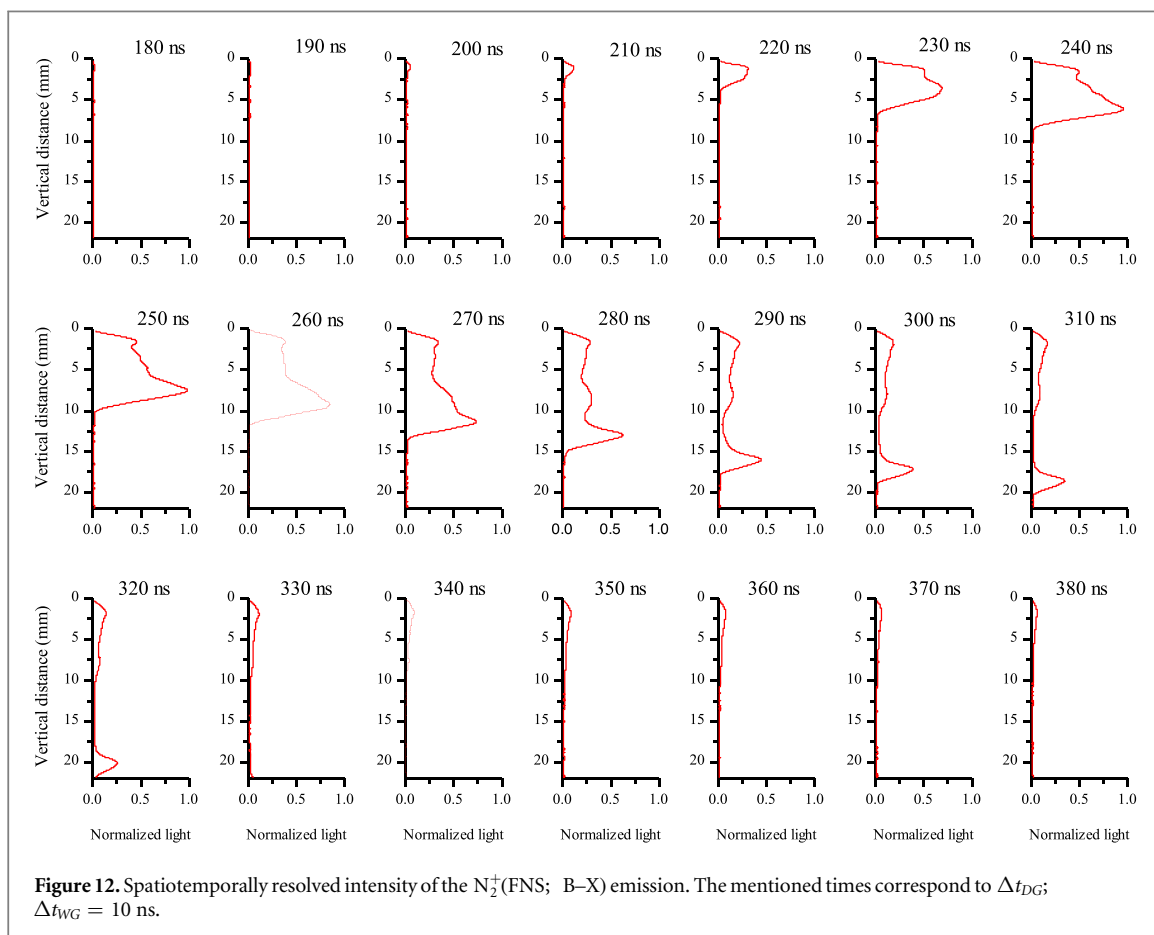
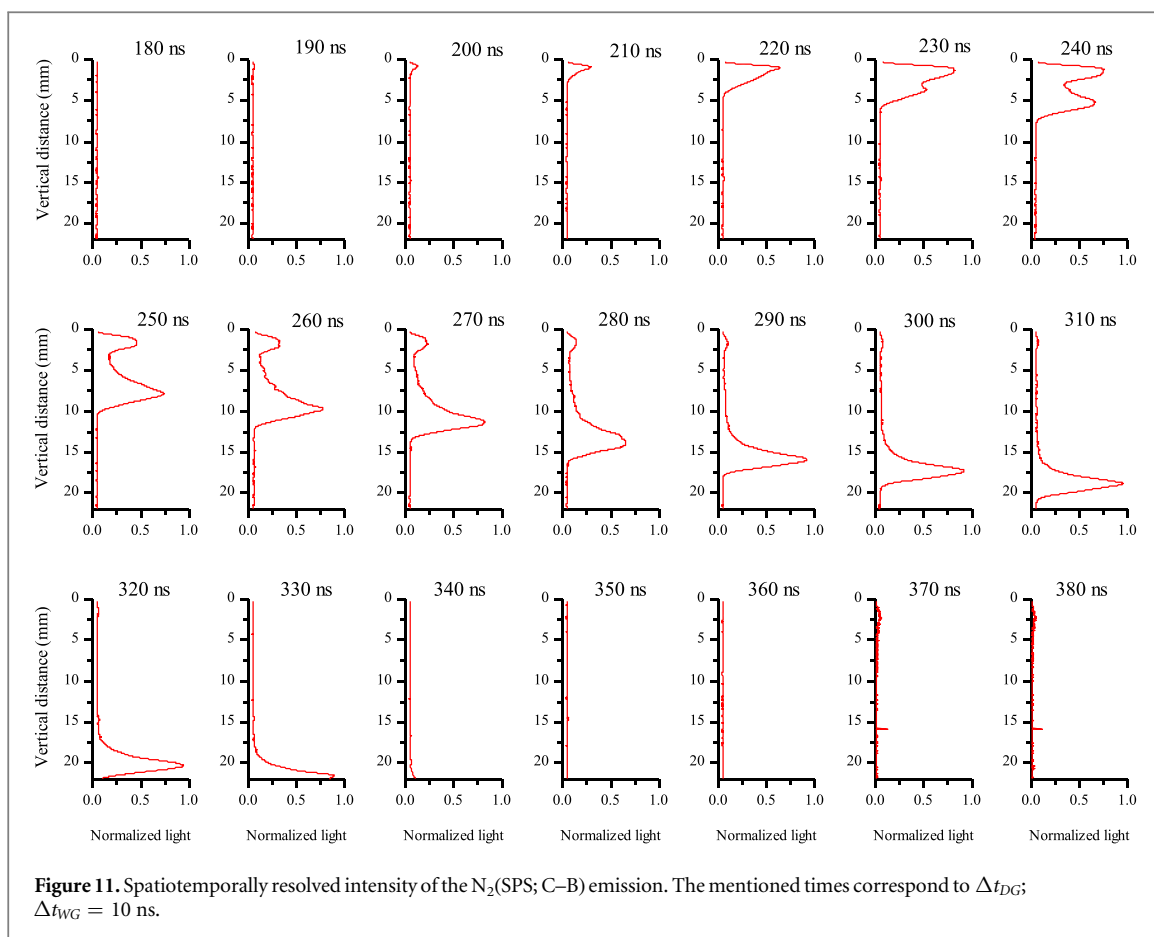
Figure 9 refers to the plots obtained by averaging the values across each row of pixels in figure 8(a) to obtain the distribution of the light intensity along the vertical axis. All values are reduced to the maximal one. These plots unveil information that could hardly be extracted by naked eye from the ICCD snapshots. Three distinct features are predominant along the propagation path: (i) a first peak closely connected to the reactor orifice at all times; (ii) a second peak emerging from the first and moving away from the reactor orifice; and (iii) a continuum which couples the two peaks as far as they there exist. It is reminded that the plots refer to the emission induced by different species and not to the direct observation of electron avalanche propagation. However, if species excitation is mainly attributed to electronic collisions with neutrals, the plots imply hidden information on the distribution of the space charge or/and the local electric field, as discussed further in section 5.

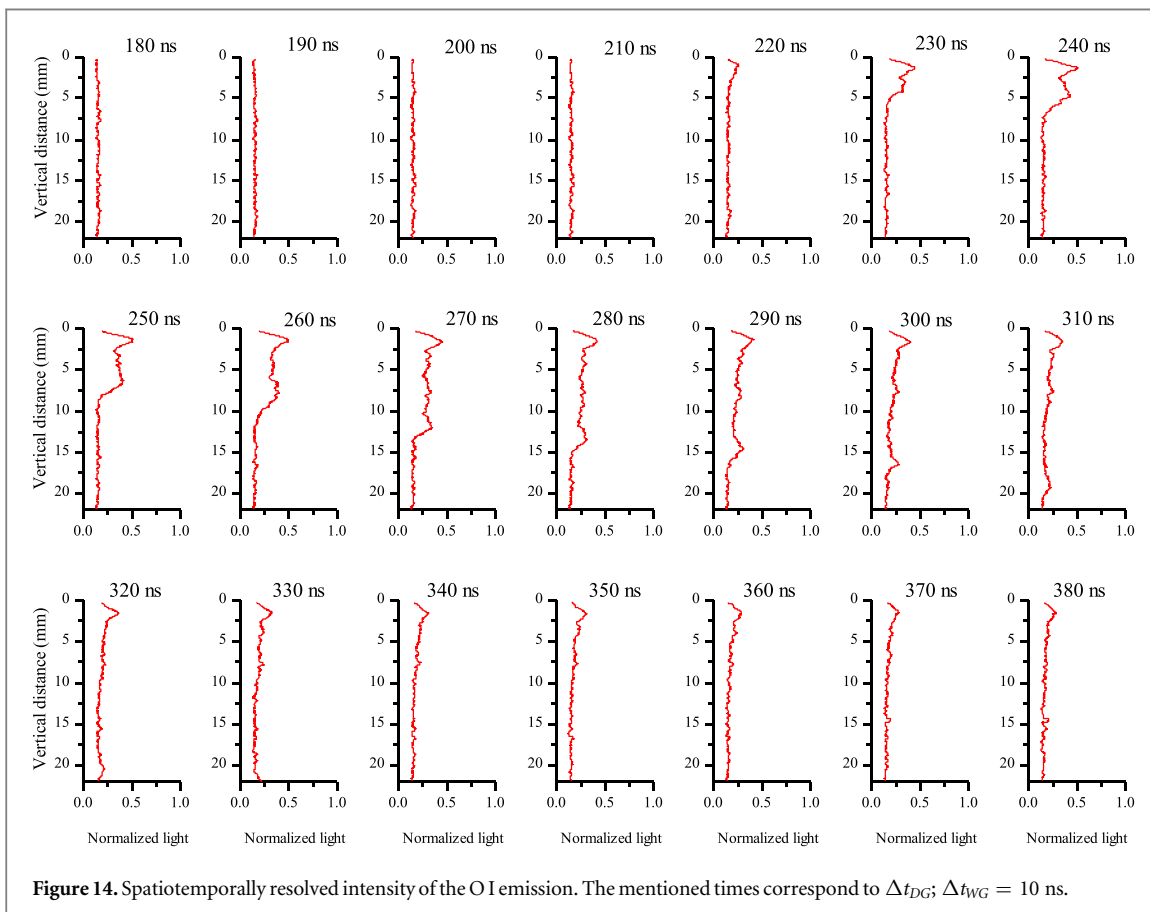
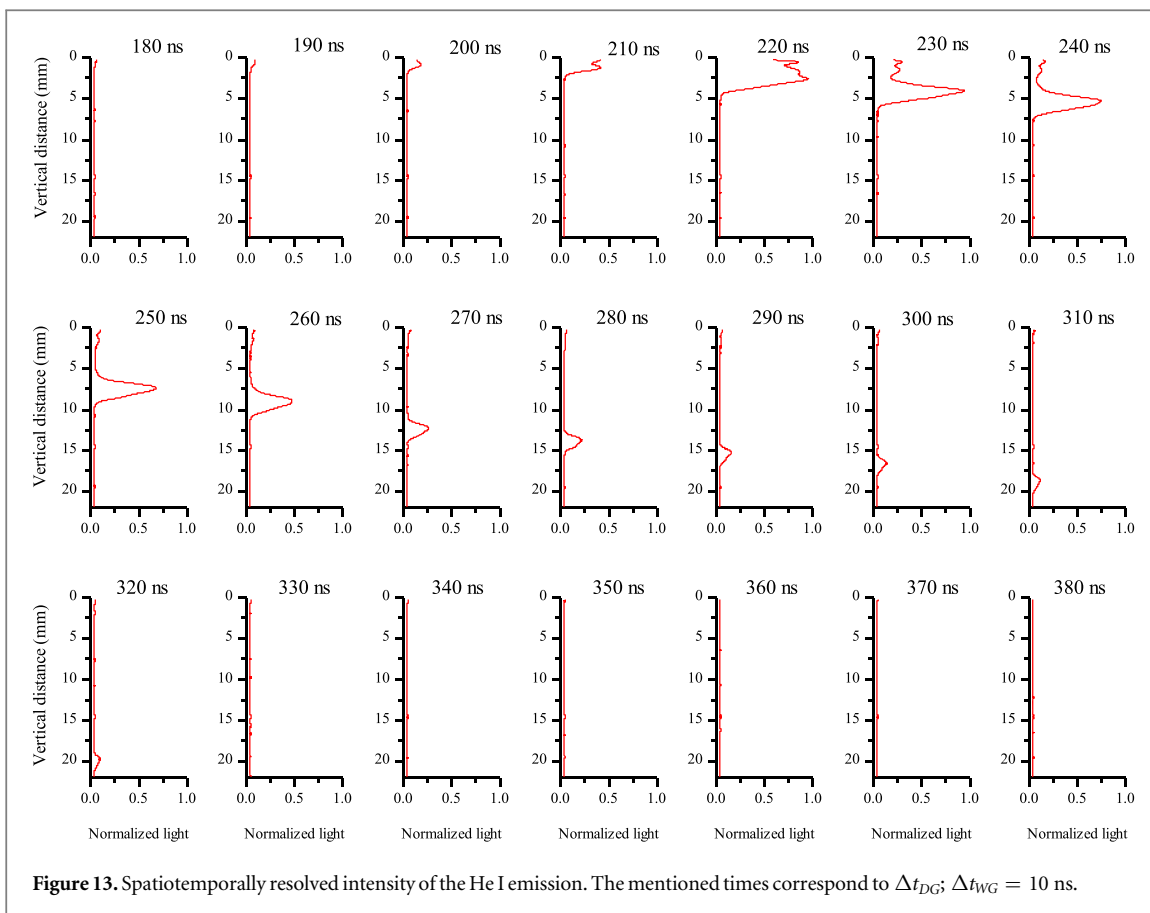
The distinct features mentioned above are also observable in the plots describing the OH(A–X) (figure 10) and N_2 (SPS; C–B) (figure 11) emissions. However, it is underlined that, despite the qualitative information that is gained from the numerical processing of the ICCD images, a one-to-one comparison between the results obtained for different species is not permissible for two main reasons: i) the optical system employed (ICCD sensor, lens, and filters) is not calibrated in terms of absolute spectral efficiency; and ii) the filtering threshold depends on the specific species under consideration. Back to figures 10 and 11, the propagating (second) peak achieves its maximum at 290 ns for OH(A–X) and 310 ns for N_2 (SPS; C–B), which implies that different reactions are responsible for the production and the destruction of those species (section 5).

Apart from the neutral emissive species, i.e., OH(A–X) and N_2 (SPS; C–B), the ionic species N_2^+ (FNS; B–X) is probed. Figure 12 presents the corresponding emission intensity. It is worth noticing that the continuum which couples the two distinct peaks demonstrates some fluctuations, and even a third intermediate peak there exists. This can be easily noticed, for instance, in the plots between 270 to 310 ns. These fluctuations are mirrored on the TL plots too (figure 9). On the top of that, the propagating peak is maximized at 250 ns, as in the TL signal case. More comments on signal features are deferred until section 5.

The last two neutral emissive species studied are He I at 706.5 nm originating in the carrier gas and O I at 777.3 nm originating in the surrounding air. Figures 13 and 14 give the respective plots. In the case of He I, the first peak is not relatively intense, and the second peak is maximal at 220 ns. In the case of O I, the moving peak appears relatively weak, while the second peak is maximal at 240 ns. It is mentioned that the signals are normalized before the moving filter application to avoid distortions as much as possible. This explains the relatively high deviation from the value of 1.0 wherever the raw data have a low signal-to-noise ratio.







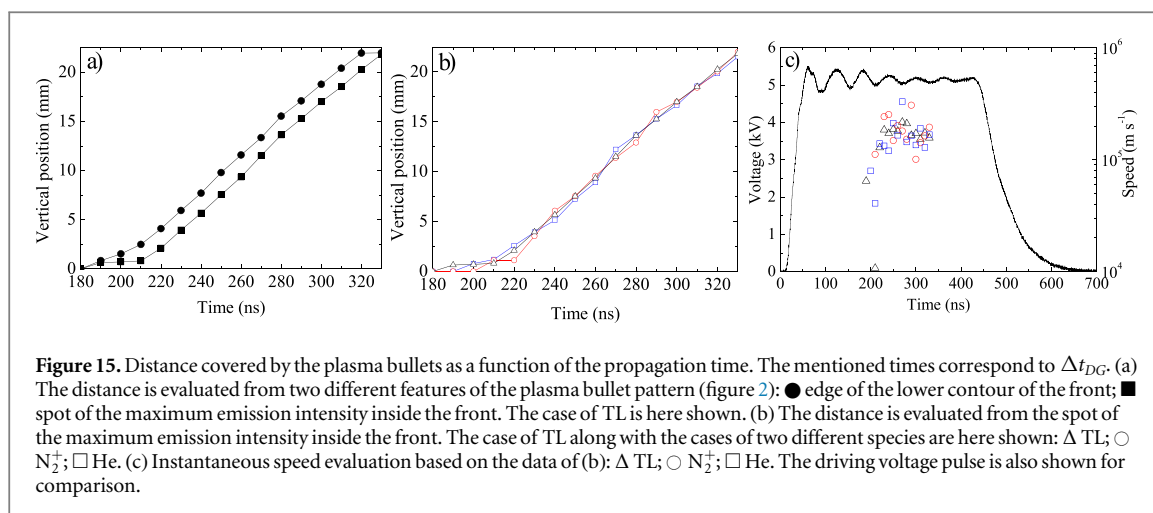


Figure 15. Distance covered by the plasma bullets as a function of the propagation time. The mentioned times correspond to Δt_{DG} . (a) The distance is evaluated from two different features of the plasma bullet pattern (figure 2): ● edge of the lower contour of the front; ■ spot of the maximum emission intensity inside the front. The case of TL is here shown. (b) The distance is evaluated from the spot of the maximum emission intensity inside the front. The case of TL along with the cases of two different species are here shown: Δ TL; \circ N_2^+ ; \square He. (c) Instantaneous speed evaluation based on the data of (b): Δ TL; \circ N_2^+ ; \square He. The driving voltage pulse is also shown for comparison.

A principal parameter that can be estimated by the above dynamic analysis is the propagation speed of the plasma bullets which is characterized by the front propagation speed. Nevertheless, the front covers a certain surface-volume and the distance that it traverses must be defined explicitly. This issue is not sufficiently discussed in most of the published works, with a few exceptions [43] where time-resolved OES has been employed for the accurate measurement of the plasma bullet speed. In the present study, different tests are conducted, and figure 15 provides indicative results.

Figure 15(a) refers to the wavelength-integrated emission (TL). It compares the distance covered by the plasma bullet versus the propagation time when two different points of the bullet pattern are processed, i.e.: (i) the edge of the lower contour of the front (figure 2) and (ii) the spot of the maximal emission intensity inside the front pattern. The resultant curves have the same tendency and close values. Similar trends and values are obtained for the individual species. Figure 15(b) makes such a comparison for the cases of the TL, He I, and N_2^+ (FNS; X-B). Thus, we may evaluate the plasma bullet instantaneous speed with reference to point ii). Indicative results are shown in figure 15(c). Values in the order of magnitude 10^5 m s^{-1} are obtained.

4.3. Fluorescent species

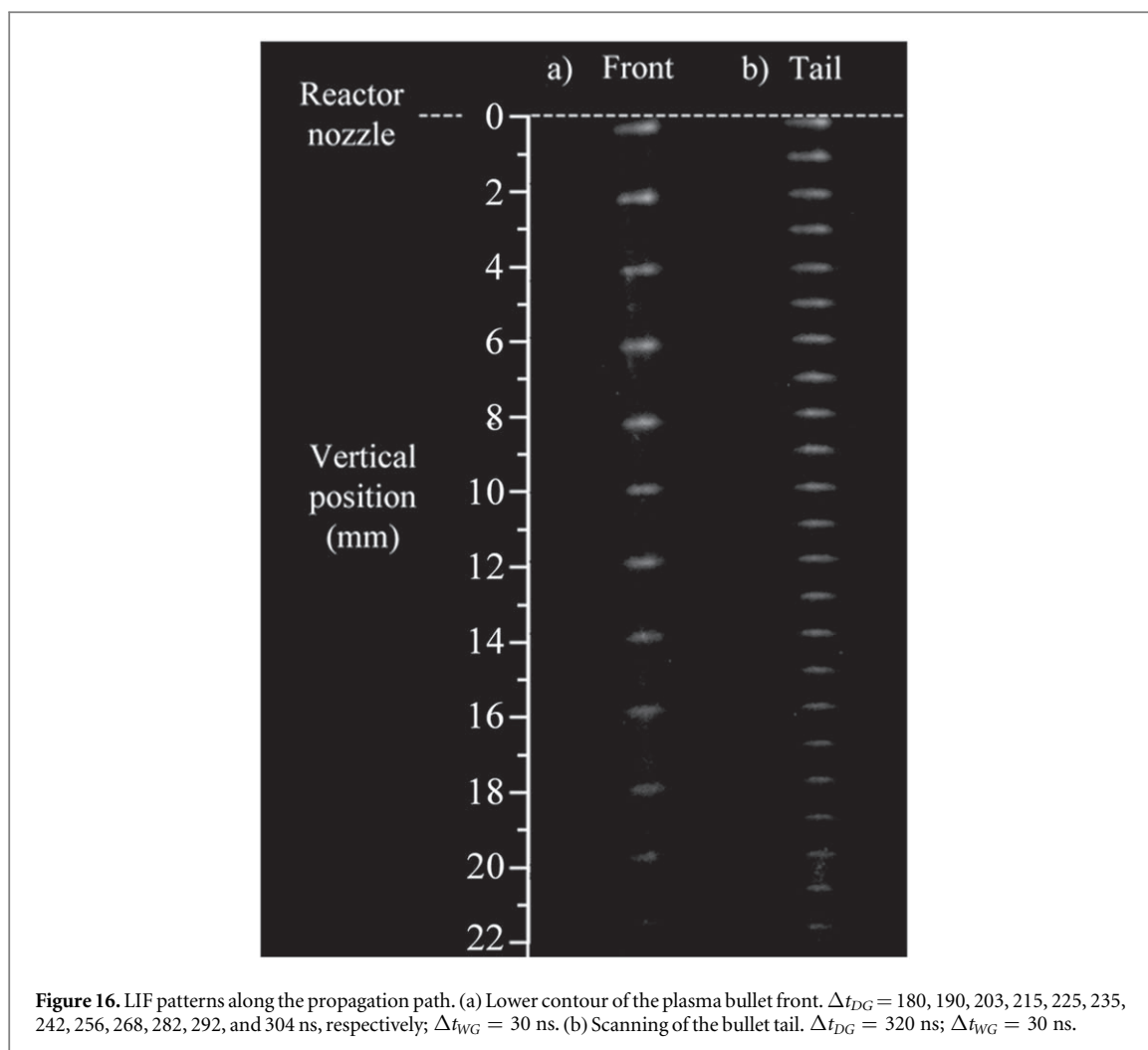
Figure 16(a) depicts the LIF intensity from the plasma bullet front (lower contour in figure 2) at various position x_i (section 2.3.1), downstream of the reactor orifice. All the successive vertical positions are increments of 2 mm. To facilitate the interpretation of these ICCD images, in figure 17(a) the LIF intensity is averaged across each row of pixels of figure 16(a) and normalized to the corresponding overall maximal value. The obtained pattern suggests a local minimum of the NO_γ relative intensity within the first about 5 mm, whereas it decreases thereafter in a quite linear manner. This fact reminds the distinction made above between the two emission peaks, close to and far from the reactor orifice.

In figure 16(b) the bullet is left to propagate for the first 320 ns to capture the whole tail within the view field of the camera and it is then scanned by means of LIF (steps of 1 mm; section 2.3.2.). Following a similar treatment with that applied to the front (figure 17(a)), figure 17(b) displays the LIF relative intensity of the NO_γ species along the bullet tail. Once again, a local minimum is clearly seen within the first 5 mm.

5. Discussion

According to the image processing results, at the dielectric/helium/air interface electric charge is built-up during about 30–40 ns, within a region of about 5 mm downstream of the reactor orifice, and a distinct ionization wave emerges and propagates thereafter. The electric charge continues to expand in terms of density, but there exist practically in a confined space, whereas the ionization wave expands and propagates. Both pass by individual maximal densities, at different times, and eventually decay. In addition, figure 15(c) shows a trend of the ionization wave speed. That is, it passes also from a maximum during the wave propagation. This fact has been previously observed by combining an ICCD and a dispersion grating [44], under conditions close to the present ones.

The ionization wave speed in the helium/air channel found to be in the order of 10^5 m s^{-1} . Streamer models based on photoionization have been proposed to explain such high speeds under low electric field [45]. The ionization wave found also to propagate inside the dielectric tube with a mean speed in the same order of magnitude, i.e., 10^5 m s^{-1} ; similar to what previous studies have shown [46].



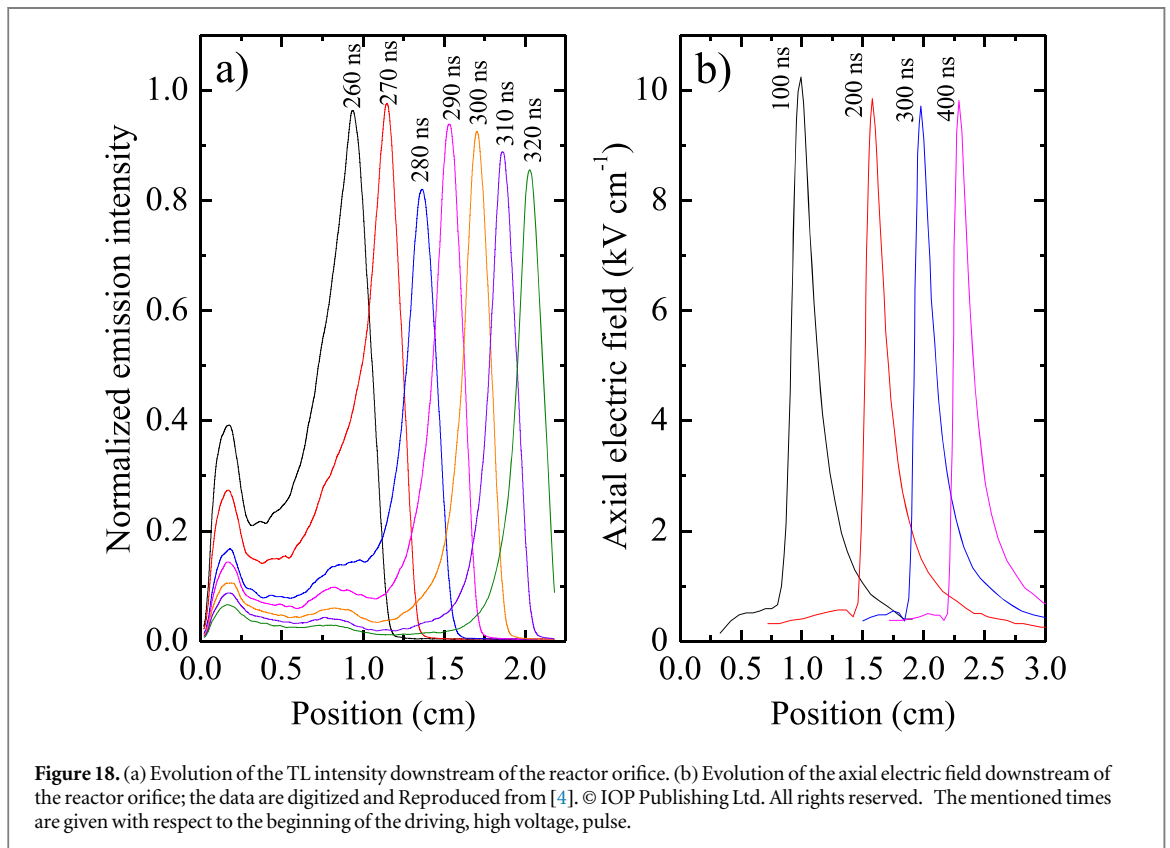
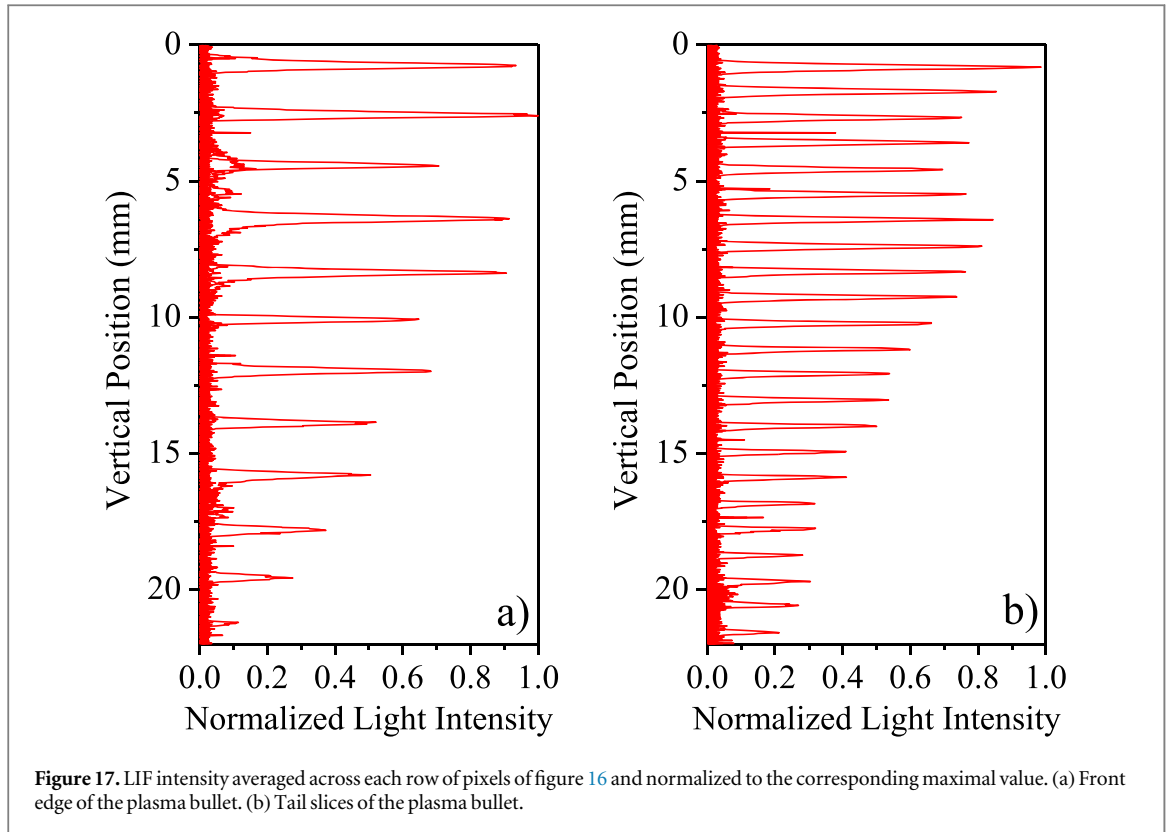
In a rough qualitative manner, figure 18 compares the experimentally recorded emission induced by the ionization wave propagation (TL case) and the numerically calculated electric field across the propagation path [4] at conditions approaching the present ones. The model main conditions refer to [4]: ring driven electrode in contact with the gas (here, internal wire electrode in contact with the gas); He gas (here, He); pulsed voltage plateau 5 kV (here, 5 kV); pulse rising time 50 ns between 1 and 5 kV (here, 31 ns); tube diameter 3 mm (here, 1.14 mm). Based on this comparison, we deal with an interplay between a propagating electric field which accounts for the ionization wave propagation, and vice versa. This leads to enhanced species production, enriching the plasma chemistry.

Starting with He I atoms, they are excited by electrons and can be depleted through various channels including spontaneous emission (e.g., $3^3S_1 \rightarrow 2^3P$; Einstein coefficient: $A = 1.54 \times 10^7 \text{ s}^{-1}$ [47]), electron impact excitation to higher levels, collision with air molecules (N_2 and O_2) and helium atoms [48].

Besides, O I atoms can be also excited by electrons. Their de-population is due to radiative relaxation to lower states (e.g., $3p^5P \rightarrow 3s^5S$; $A = 3.69 \times 10^7 \text{ s}^{-1}$ [47]), excitation to more energetic levels, quenching by N_2/O_2 , and production of ozone: $O(3p^5P) + O_2 + H_2O \rightarrow O_3 + H_2O$ (rate constant: $k = 9.9 \times 10^{-34} e^{510/T} \text{ cm}^6 \text{ s}^{-1}$, for a temperature T in the range 300 to 800 K [49]; T is expected to be slightly higher than 300 K in the present study [37]).

The population of OH(A) in the present plasma jet should be due to electron-impact dissociative excitation of H_2O (present in the form of vapour in the surrounding air): $e^- + H_2O \rightarrow OH(A) + H + e^-$ [37]. Then, depletion of OH(A) takes place via radiative relaxation to its ground state (i.e., $OH(A) \rightarrow OH(X) + h\nu$; $A = 1.25 \times 10^6 \text{ s}^{-1}$ [50]) and through collisional quenching by N_2/O_2 , as follows: $OH(A) + N_2/O_2 \rightarrow \text{products}$ with $k_{N_2} = 3.2 \times 10^{-11} \text{ cm}^3 \text{ s}^{-1}$ and $k_{O_2} = 7 \times k_{N_2}$ [37].

The excitation of nitrogen molecules to the $N_2(C)$ level is done through electron impact and metastable pooling reactions ($N_2(A) + N_2(A) \rightarrow N_2(C) + N_2(X)$; $k = (1.5 - 3) \times 10^{-10} \text{ cm}^3 \text{ s}^{-1}$ [51, 52]). On the other hand, the $N_2(C)$ depletion is due to spontaneous emission (i.e., $N_2(C) \rightarrow N_2(B) + h\nu$; $A = 2.74 \times 10^7 \text{ s}^{-1}$ [50]) and quenching by He and N_2/O_2 according to the following channels:



$\text{N}_2(\text{C}) + \text{He} \rightarrow \text{products}$ ($k_{\text{He}} = 9.3 \times 10^{-12} \text{cm}^3 \text{s}^{-1}$), $\text{N}_2(\text{C}) + \text{N}_2/\text{O}_2 \rightarrow \text{products}$ ($k_{\text{N}_2} = 1.17 \times k_{\text{He}}$; $k_{\text{O}_2} = 0.47 \times k_{\text{He}}$ [37]), and $\text{N}_2(\text{C}) + \text{O}_2 \rightarrow \text{N}_2(\text{A}) + \text{O} + \text{O}(\text{^1S})$ ($k_{\text{O}_2} = 3 \times 10^{-10} \text{cm}^3 \text{s}^{-1}$ [53]).

Furthermore, nitrogen ions can be produced via electron impacts, Penning ionization with helium metastables (He^m) and charge transfer reactions with helium dimer ions (He_2^+), as follows: $\text{He}^m + \text{N}_2(\text{X}) \rightarrow \text{N}_2^+(\text{B}) + \text{He}$ ($k = 7.1 \times 10^{-11} \text{cm}^3 \text{s}^{-1}$ [51]) and $\text{He}_2^+ + \text{N}_2(\text{X}) \rightarrow \text{N}_2^+(\text{B}) + 2\text{He}$ ($k = 8.3 \times 10^{-10} \text{cm}^3 \text{s}^{-1}$ [54]). On the other hand, the $\text{N}_2^+(\text{B})$ state is depleted through spontaneous emission (i.e., $\text{N}_2^+(\text{B}) \rightarrow \text{N}_2^+(\text{X}) + h\nu$; $A = 1.5 \times 10^7 \text{s}^{-1}$ [54]) and quenched by N_2/O_2 : $\text{N}_2^+(\text{B}) + \text{N}_2/\text{O}_2 \rightarrow \text{products}$ with $k_{\text{N}_2} = 2.1 \times 10^{-10} \text{cm}^3 \text{s}^{-1}$ and $k_{\text{O}_2} = 2.43 \times k_{\text{N}_2}$ [37]. Particularly, Penning ionization is a crucial ionization process for $\text{N}_2(\text{X})$ in helium plasma jets leading to the creation of $\text{N}_2^+(\text{B})$ ions along the jet axis. These are unambiguously present here as revealed by their fingerprint, i.e., $\text{N}_2^+(\text{FNS})$ emission at 391.4 nm. Thus, an enhanced creation of nitrogen ions after the exit of the tube takes place. It leads to an enhancement of the local electric field as it is suggested by the increasing speed of the ionization wave up to a certain distance after the tube's exit. The particular structure of the continuum of the $\text{N}_2^+(\text{B})$ emission, e.g., between 270 and 310 ns in figure 12, may be attributed to this enhancement of the local electric field.

Finally, the NO_γ fluorescence is studied in figures 16 and 17, following laser-induced excitation of $\text{NO}(\text{X})$ to the $\text{NO}(\text{A})$ state. Besides, in the present plasma jet $\text{NO}(\text{A})$ should be populated via electron impacts with $\text{NO}(\text{X})$ (i.e., $e^- + \text{NO}(\text{X}) \rightarrow \text{NO}(\text{A}) + e^-$; $k = 2 \times 10^{-10} \text{cm}^3 \text{s}^{-1}$ [55]) and is depleted through the following channels: $\text{NO}(\text{A}) \rightarrow \text{NO}(\text{X}) + h\nu$ ($A = 4.59 \times 10^6 \text{s}^{-1}$) and $\text{NO}(\text{A}) + \text{N}_2/\text{O}_2 \rightarrow \text{products}$ with $k_{\text{N}_2} = 4.7 \times 10^{10} \text{cm}^3 \text{mol}^{-1} \text{s}^{-1}$ and $k_{\text{O}_2} = 9.09 \times 10^{13} \text{cm}^3 \text{mol}^{-1} \text{s}^{-1}$ [56].

From the abovementioned spontaneous emission coefficients A_i , the natural lifetime ($\tau_{\text{nat}_i} = 1/A_i$) of $\text{He}(3^3\text{S}_1)$ is $\tau_{\text{nat}_{\text{He}}} = 64.6$ ns. Similarly, for $\text{O}(3\text{p}^5\text{P})$, $\text{OH}(\text{A})$, $\text{N}_2(\text{C})$, $\text{N}_2^+(\text{B})$ and $\text{NO}(\text{A})$ we obtain $\tau_{\text{nat}_{\text{O}}} = 27.1$ ns, $\tau_{\text{nat}_{\text{OH}}} = 800$ ns, $\tau_{\text{nat}_{\text{N}_2}} = 36.4$ ns, $\tau_{\text{nat}_{\text{N}_2^+}} = 66.6$ ns and $\tau_{\text{nat}_{\text{NO}}} = 217$ ns, respectively. If we also consider the rate constants (k) for quenching of these states by atoms and molecules, their lifetimes become even lower [37]. This is due to additional depletion processes, leading to much lower effective lifetimes τ_{eff} , with $1/\tau_{\text{eff}} = 1/\tau_{\text{nat}} + k \times [C_q]$, $[C_q]$ being the density of a quencher such as N_2 or O_2 .

Based on figures 11–14, and as it was indicated in section 4.2, the maximum intensity of the propagating (second) peak of $\text{N}_2(\text{SPS})$, $\text{N}_2^+(\text{FNS})$, He I , and O I , is obtained at 310, 250, 220, and 240 ns, respectively, while all emissions are still detectable for times equal or higher than 320 ns. For the case of the $\text{N}_2(\text{C})$, $\text{N}_2^+(\text{B})$, $\text{He}(3^3\text{S}_1)$, and $\text{O}(3\text{p}^5\text{P})$ species, it would be expected that $\tau_{\text{eff}} \ll 40$ ns [37]. Thus, the results of figures 11–14 suggest that additional production channels of these excited states should be present up to at least 20 mm away from the reactor orifice. This observation agrees with figure 18(b) where the local electric field is sustained for long times. For the case of the $\text{OH}(\text{A})$ and $\text{NO}(\text{A})$ species, the optical emission and LIF intensity extinguishes at much shorter times (figures 10 and 17) as compared with their natural lifetimes, being 800 and 217 ns respectively. This mirrors the complex depletion paths that should be considered in a dedicated relative study.

6. Conclusions

Over the last decades, fast imaging has widely been combined with bandpass optical filters and laser-induced fluorescence for the study of dynamic effects occurring at atmospheric pressure cold plasmas. However, the present work claimed that these diagnostics should be coupled with image processing numerical techniques to elicit more informative data. The proof of this concept was achieved by considering a helium pulsed plasma jet and probing the spatiotemporal evolution of various species (N_2 , N_2^+ , He , OH , O , and NO_γ), along the propagation path of ionization waves. Two distinct regions of reactive species formation along the propagation path were found. The first region was located close to the reactor orifice and the second region referred to the variable position of ionization waves. The latter achieved a propagation speed up to $2 \times 10^5 \text{m s}^{-1}$. Finally, it was demonstrated that the emission patterns of representative species may contain inherent information related to the profile of other physical quantities, like the local electric field.

Acknowledgments

The Authors would like to thank Dr Rodney Bowersox and his Group at Texas A&M for sharing scientific equipment necessary to perform the study presented in this manuscript. A. G. is supported by the Luxembourg National Research Fund 15480342 (FRAGOLA).

Data availability statement

The data cannot be made publicly available upon publication because they are not available in a format that is sufficiently accessible or reusable by other researchers. The data that support the findings of this study are available upon reasonable request from the authors.

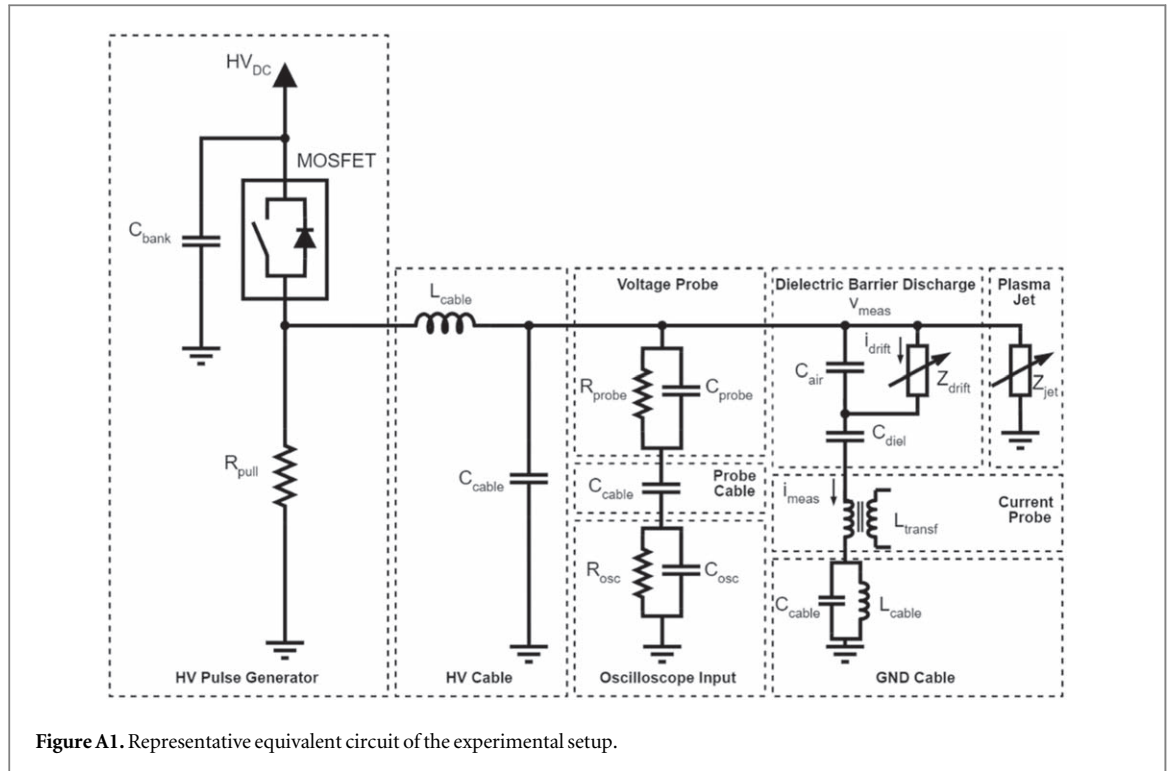


Figure A1. Representative equivalent circuit of the experimental setup.

Appendix

Many reports consider equivalent electrical circuits for the DBD-based reactors [57–60]. Figure A1 provides a representative such circuit for the present experimental setup, including stray electrical components. In the frames of ‘Dielectric Barrier Discharge’—‘Current Probe’, both $v_{meas}(t)$ and $i_{meas}(t)$ are experimentally determined (figures 1 and 5). Thus, the drift current of the discharge, $i_{drift}(t)$, can be evaluated by considering rational values of the capacitances formed by the air gap and the dielectric barrier (C_{air} and C_{diel} , respectively). These capacitances have coaxial geometry, defined radii (section 2.1), and known dielectric constants ($\epsilon_{r_air} = 1$ and $\epsilon_{r_diel} = 9.5 \pm 7\%$). Furthermore, the length of these capacitances is about 10 mm (figure 1), while the radii involved in the geometry are between 0.0625 to 1.25 mm (section 2.1). Consequently, the traditional formula for a coaxial capacitance of infinite length can fairly be used, leading to the values $C_{air} = 0.25$ pF and $C_{diel} = 6.74 \pm 7\%$ pF.

On the other hand, by ignoring the stray impedance ‘seen’ by the primary winding of the ‘Current Probe’ and the stray impedance due to the short ‘GND Cable’ (figure A1), and solving for the DBD current, the following equation is obtained:

$$i_{drift}(t) = \left(1 + \frac{C_{air}}{C_{diel}}\right) i_{meas}(t) - C_{air} \frac{dv_{meas}(t)}{dt} \quad (1)$$

The last term of equation (1) is calculated by taking numerically the derivative of the measured voltage waveform, while the rest terms are known. The result is illustrated in figure 5.

ORCID iDs

D K Athanasopoulos <https://orcid.org/0000-0001-6071-2884>

P Svarnas <https://orcid.org/0000-0002-2818-744X>

P K Papadopoulos <https://orcid.org/0000-0001-7472-5416>

K Gazeli <https://orcid.org/0000-0002-5479-0373>

K Giotis <https://orcid.org/0000-0002-8615-331X>

P Vafeas <https://orcid.org/0000-0002-0896-4168>

G P Vafakos <https://orcid.org/0000-0001-8248-4472>

A Gerakis <https://orcid.org/0000-0002-3356-2304>

References

- [1] Lu X, Naidis G V, Laroussi M, Reuter S, Graves D B and Ostrikov K 2016 Reactive species in non-equilibrium atmospheric-pressure plasmas: generation, transport, and biological effects *Phys. Rep.* **630** 1–84
- [2] Svarnas P, Gazeli K, Gkelios A, Amanatides L and Mataras D 2018 On the reliable probing of discrete ‘plasma bullet’ propagation *Meas. Sci. Technol.* **29** 045016
- [3] von Woedtke T, Reuter S, Masura K and Weltmann K-D 2013 Plasmas for medicine *Phys. Rep.* **530** 291
- [4] Boeuf J-P, Yang L L and Pitchford L C 2013 Dynamics of a guided streamer (‘plasma bullet’) in a helium jet in air at atmospheric pressure *J. Phys. D: Appl. Phys.* **46** 015201
- [5] Walsh J L, Shi J J and Kong M G 2006 Contrasting characteristics of pulsed and sinusoidal cold atmospheric plasma jets *App. Phys. Lett.* **88** 171501
- [6] Svarnas P, Romadanov I, Diallo A and Raites Y 2018 Velocity distribution functions of Xe I and Xe II in ambipolar plasma flow using a single tunable diode laser *IEEE Trans. Plasma Sci.* **46** 3998
- [7] Yonemori S and Ono R 2014 Flux of OH and O radicals onto a surface by an atmospheric-pressure helium plasma jet measured by laser-induced fluorescence *J. Phys. D: Appl. Phys.* **47** 125401
- [8] Riès D, Dilecce G, Robert E, Ambrico F P, Dozias S and Pouvesle J-M 2014 LIF and fast imaging plasma jet characterization relevant for NTP biomedical applications *J. Phys. D: Appl. Phys.* **47** 275401
- [9] Yue Y, Pei X, Gidon D, Wu F, Wu S and Lu X 2018 Investigation of plasma dynamics and spatially varying O and OH concentrations in atmospheric pressure plasma jets impinging on glass, water and metal substrates *Plasma Sources Sci. Technol.* **27** 064001
- [10] Yang Y, Zhang Y, Liao Z, Pei X and Wu S 2018 OH radicals distribution and discharge dynamics of an atmospheric pressure plasma jet above water surface *IEEE Trans. Radiat. Plasma Med. Sci.* **2** 223
- [11] Wu F, Li J, Liu F, Zhou X and Lu X 2018 The effect of skin moisture on the density distribution of OH and O close to the skin surface *J. Appl. Phys.* **123** 123301
- [12] Song S, Sözer B E and Jiang C 2019 Effects of pulse width on He plasma jets in contact with water evaluated by OH(A–X) emission and OH_{aq} production *Jpn. J. Appl. Phys.* **58** 066002
- [13] Urabe K, Sands L B, Ganguly N B and Sakai O 2012 Temporally and spectrally resolved observation of a crossed-flow DBD plasma jet using pure helium and argon/acetone mixed gases *Plasma Sources Sci. Technol.* **21** 034004
- [14] Leiweke J R, Ganguly N B and Scofield D J 2014 Voltage and pressure scaling of streamer dynamics in a helium plasma jet with N₂ co-flow *Phys. Plasmas* **21** 083508
- [15] Urabe K, Morita T, Tachibana K and Ganguly B N 2010 Investigation of discharge mechanisms in helium plasma jet at atmospheric pressure by laser spectroscopic measurements *J. Phys. D: Appl. Phys.* **43** 095201
- [16] Yonemori S, Nakagawa Y, Ono R and Oda T 2012 Measurement of OH density and air-helium mixture ratio in an atmospheric-pressure helium plasma jet *J. Phys. D: Appl. Phys.* **45** 225202
- [17] Ono R and Tokuhiro M 2020 Spatiotemporal measurement of OH density from upstream to downstream in humid helium atmospheric-pressure plasma jet *Plasma Sources Sci. Technol.* **29** 035021
- [18] Pei X, Lu Y, Wu S, Xiong Q and Lu X 2013 A study on the temporally and spatially resolved OH radical distribution of a room-temperature atmospheric-pressure plasma jet by laser-induced fluorescence imaging *Plasma Sources Sci. Technol.* **22** 025203
- [19] Pei X, Wu S, Xian Y, Lu X and Pan Y 2014 On OH density of an atmospheric pressure plasma jet by laser-induced fluorescence *IEEE Trans. Plasma Sci.* **42** 5
- [20] Yue Y, Pei X and Lu X 2016 OH density optimization in atmospheric-pressure plasma jet by using multiple ring electrodes *J. Appl. Phys.* **119** 033301
- [21] Yue Y, Jiang J, Kondeti V S S K and Bruggeman J P 2021 Spatially and temporally resolved H and OH densities in a nanosecond pulsed plasma jet: an analysis of the radical generation, transport, recombination and memory effects *J. Phys. D: Appl. Phys.* **54** 115202
- [22] Xiong Q et al 2009 Temporal and spatial resolved optical emission behaviors of a cold atmospheric pressure plasma jet *J. Appl. Phys.* **106** 083302
- [23] Qiao J, Zhang L, Yang D, Jia Z, Song Y, Zhao Z, Yuan H, Xia Y and Wang W 2019 Temporal evolution of the relative vibrational population of N₂(C³Π_u) and optical emission spectra of atmospheric pressure plasma jets in He mixtures *J. Phys. D: Appl. Phys.* **52** 285203
- [24] Gott P R and Xu G K 2020 Time-resolved imaging and spectroscopy of atmospheric pressure plasma bullet propagation and RONS production *J. Phys. D: Appl. Phys.* **53** 315201
- [25] Svarnas P, Spiliopoulou A, Koutsoukos P G, Gazeli K and Anastassiou E D 2019 Acinetobacter baumannii deactivation by means of DBD-based helium plasma jet *Plasma* **2** 77
- [26] Athanasopoulos D, Svarnas P, Ladas S, Kennou S and Koutsoukos P 2018 On the wetting properties of human stratum corneum epidermidis surface exposed to cold atmospheric-pressure pulsed plasma *Appl. Phys. Lett.* **112** 213703
- [27] Svarnas P, Matrali S H, Gazeli K and Antimisariaris S G 2015 Assessment of atmospheric-pressure guided streamers (plasma bullet) influence on liposomes with different composition and physicochemical properties *Plasma Process. Polym.* **12** 655
- [28] Svarnas P, Matrali S H, Gazeli K, Aleiferis S P, Clément F and Antimisariaris S G 2012 Atmospheric-pressure guided streamers for liposomal membrane disruption *Appl. Phys. Lett.* **101** 264103
- [29] Papadopoulos P K, Vafeas P, Svarnas P, Gazeli K, Hatzikonstantinou P M, Gkelios A and Clément F 2014 Interpretation of the gas flow field modification induced by guided streamer (‘plasma bullet’) propagation *J. Phys. D: Appl. Phys.* **47** 425203
- [30] Papadopoulos P K, Athanasopoulos D, Sklias K, Svarnas P, Mourousias N, Vratisinis K and Vafeas P 2019 Generic residual charge based model for the interpretation of the electrohydrodynamic effects in cold atmospheric pressure plasmas *Plasma Sources Sci. Technol.* **28** 065005
- [31] Logothetis D K, Papadopoulos P K, Svarnas P and Vafeas P 2016 Numerical simulation of the interaction between helium jet flow and an atmospheric-pressure ‘plasma jet’ *Comput. Fluids* **140** 11
- [32] Giotis K, Svarnas P, Petrou K, Poupouzas M and Athanasopoulos D K 2022 Cockcroft-Walton generator: an effective voltage multiplier for power supplies of square pulses driving DBD plasmas *IEEE Trans. Plasma Sci.* **50** 2185
- [33] Koliadimas A, Apostolopoulos D, Svarnas P, Sklias K, Athanasopoulos D and Mitronikas E 2019 A microcontroller based modular pulsed H.V. power supply: design, implementation and tests on DBD-based plasmas *IEEE Trans. Plasma Sci.* **47** 1621
- [34] Athanasopoulos D, Svarnas P and Gerakis A 2019 Cold plasma bullet influence on the water contact angle of human skin surface *J. Electrostat.* **102** 103378
- [35] Gazeli K, Svarnas P, Lazarou C, Anastassiou C, Georghiou G E, Papadopoulos P and Clément F 2020 Microsecond pulsed atmospheric pressure helium plasma jet: a parametric study based on UV-to-NIR observations *Phys. Plasmas* **27** 123503

- [36] Gazeli K, Svarnas P, Held B, Marlin L and Clément F 2015 Possibility of controlling the chemical pattern of He and Ar 'guided streamers' by means of N₂ or O₂ additives *J. Appl. Phys.* **117** 093302
- [37] Gazeli K, Nöel C, Clément F, Daugé C, Svarnas P and Belmonte T 2013 A study of helium atmospheric-pressure guided streamer for potential biological applications *Plasma Sources Sci. Technol.* **22** 025020
- [38] Gherardi M, Puač N, Marić D, Stancampiano A, Malović G, Colombo V and Petrović Z L 2015 Practical and theoretical considerations on the use of ICCD imaging for the characterization of non-equilibrium plasmas *Plasma Sources Sci. Technol.* **24** 064004
- [39] Girard F, Badets V, Blanc S, Gazeli K, Marlin L, Authier L, Svarnas P, Sojic N, Clément F and Arbault S 2016 Formation of reactive nitrogen species including peroxyxynitrite in physiological buffer exposed to a cold atmospheric plasma *RSC Adv.* **6** 78457
- [40] Gessel H F A, Hrycak B, Jasiński M, Mizeraczyk J, Mullen M A J J and Bruggeman J P 2013 Temperature and NO density measurements by LIF and OES on an atmospheric pressure plasma jet *J. Phys. D: Appl. Phys.* **46** 095201
- [41] Yagi I, Shirakawa Y, Hirakata K, Akiyama T, Yonemori S, Mizuno K, Onol R and Oda T 2015 Measurement of OH, O, and NO densities and their correlations with mouse melanoma cell death rate treated by a nanosecond pulsed streamer discharge *J. Phys. D: Appl. Phys.* **48** 424006
- [42] Gazeli K, Svarnas P, Vafeas P, Papadopoulos P K, Gkelios A and Clément F 2013 Investigation on streamers propagating into a helium jet in air at atmospheric pressure: electrical and optical emission analysis *J. Appl. Phys.* **114** 103304
- [43] Karakas E and Laroussi M 2010 Experimental studies on the plasma bullet propagation and its inhibition *J. Appl. Phys.* **108** 063305
- [44] Xiong Q *et al* 2010 Experimental investigations on the propagation of the plasma jet in the open air *J. Appl. Phys.* **107** 073302
- [45] Lu X and Laroussi M 2006 Dynamics of an atmospheric pressure plasma plume generated by submicrosecond voltage pulses *J. Appl. Phys.* **100** 063302
- [46] Bourdon A, Darny T, Pechereau F, Pouvesle J-M, Viegas P, Iséni S and Robert E 2016 Numerical and experimental study of the dynamics of a μ s helium plasma gun discharge with various amounts of N₂ admixture *Plasma Sources Sci. Technol.* **25** 035002
- [47] NIST Atomic Database (<https://nist.gov/pml/atomic-spectra-database>)
- [48] Belmonte T, Cardoso R P, Henrion G and Kosior F 2007 Collisional–radiative modelling of a helium microwave plasma in a resonant cavity *J. Phys. D: Appl. Phys.* **40** 7343
- [49] Peyroux R, Pignolet P and Held B 1989 Kinetic simulation of gaseous species created by an electrical discharge in dry or humid oxygen *J. Phys. D: Appl. Phys.* **22** 1658
- [50] Xiong Q, Nikiforov A Y, Lu X P and Leys C 2010 High-speed dispersed photographing of an open-air argon plasma plume by a grating–ICCD camera system *J. Phys. D: Appl. Phys.* **43** 415201
- [51] Bibinov N K, Fateev A A and Wiesemann K 2001 On the influence of metastable reactions on rotational temperatures in dielectric barrier discharges in He–N₂ mixtures *J. Phys. D: Appl. Phys.* **34** 1819
- [52] Sá P A and Loureiro J 1997 A time-dependent analysis of the nitrogen afterglow in N₂ and N₂–Ar microwave discharges *J. Phys. D: Appl. Phys.* **30** 2320
- [53] Ricard A, Czerwiec T, Belmonte T, Bockel S and Michel H 1999 Detection by emission spectroscopy of active species in plasma surface processes *Thin Solid Films* **341** 1
- [54] Bibinov N K, Fateev A A and Wiesemann K W 2001 Variations of the gas temperature in He/N₂ barrier discharges *Plasma Sources Sci. Technol.* **10** 579
- [55] Brandenburg R, Maiorov V A, Golubovskii Y B, Wagner H-E, Behnke J and Behnke J 2005 Diffuse barrier discharges in nitrogen with small admixtures of oxygen: discharge mechanism and transition to the filamentary regime *J. Phys. D: Appl. Phys.* **38** 2187
- [56] Zhao G-B, Argyle M D and Radosz M 2007 Optical emission study of nonthermal plasma confirms reaction mechanisms involving neutral rather than charged species *J. Appl. Phys.* **101** 033303
- [57] Laroussi M and Lu X 2004 Power consideration in the pulsed dielectric barrier discharge at atmospheric pressure *J. Appl. Phys.* **96** 3028
- [58] Florez D, Schitz D, Piquet H and Diez R 2018 Efficiency of an exciplex DBD lamp excited under different methods *IEEE Trans. Plasma Sci.* **46** 140
- [59] Monge-Daugé C, Clément F, Svarnas P, Loiseau J-F, Ricard A and Held B 2012 Experimental study coupled with electrical modeling for the consideration of DBD-based plasma jet *IEEE Trans. Plasma Sci.* **40** 2254
- [60] Pipa A V, Koskulics J, Brandenburg R and Hoder T 2012 The simplest equivalent circuit of a pulsed dielectric barrier discharge and the determination of the gas gap charge transfer *Rev. Sci. Instrum.* **83** 115112